GALLAWAY, DOUGLAS, Ph.D. 3D Modeling of Ultra-High-Resolution UAV Imagery using Low-Cost Photogrammetric Software and Structure from Motion. (2018)
Directed by Dr. Roy S. Stine. 116 pp.

The availability of advanced low-cost unmanned aerial systems (UASs), aftermarket applications, and a competitive market for processing software have provided researchers new opportunities for employing high resolution remote sensing in research. The UAS allows for the capture of close range aerial imagery that can then be used to generate dense point clouds using structure from motion (SfM). A variety of digital products can be created form these dense point clouds such as three-dimensional models, digital elevation models (DEMs), digital surface models (DSMs) and orthomosaics. This dissertation looks at methods and accuracies associated with the creation of digital mapping products from dense point clouds generated from imagery captured by two low-cost off the shelf UASs.

The UASs were used to capture imagery over a 2-hectare vineyard in the Uwharrie mountains of North Carolina. Aspects of imagery collection, such as altitude, ground control, camera types, flight paths, and target styles, were investigated for their impacts on accuracy. Thirty-one ground control points were created in the vineyard using a survey grade GNSS receiver and total station for use in georeferencing. The number of ground control points used for georeferencing were reduced until a significant difference in accuracy was found using t-tests.

Five ground control points were shown to be the least amount of ground control needed before accuracy began to change significantly. Four flight altitudes were tested with 80-meters generating the least level of error. Orthomosaics created from structure from motion and imagery collected using a global shutter 20-megapixel had total RMS errors between 2-4 cm.

3D MODELING OF ULTRA-HIGH-RESOLUTION UAV IMAGERY USING LOW-COST PHOTOGRAMMETRIC SOFTWARE AND STRUCTURE FROM MOTION

by

Douglas Gallaway

A Dissertation Submitted to
the Faculty of The Graduate School
The University of North Carolina at Greensboro
in Partial Fulfillment
of the Requirements for the Degree
Doctor of Philosophy

Greensboro
2018

Approved by

Roy S. Stine
Committee Chair

APPROVAL PAGE

This dissertation written by Douglas Gallaway has been approved by the following committee of the Faculty of The Graduate School at The University of North Carolina at Greensboro.

Committee Chair	Roy S. Stine
Committee Members	Phillip D. Royall
	Elisabeth S. Neslon
	Jerry W. Nave

May 29, 2018
Date of Acceptance by Committee

May 29, 2018
Date of Final Oral Examination

ACKNOWLEDGEMENTS

This dissertation would not have been possible without the guidance, experience, knowledge and support of a large number of people. I am greatly appreciative of my mentor and advisor, Dr. Roy Stine. His devotion and support to the topic of remote sensing and my research has kept me moving forward through this process. His sage, yet hilarious advice he gave when I was nervously preparing for my comps and asked him for advice will forever be burned into my head, ‘study long, study hard, and study often’. His humor and expertise have been an incredible driving force for me.

I would also like to thank my committee members who have also had a strong influence on me: Dr. Jerry Nave, Dr. Dan Royall, and Dr. Elisabeth Nelson. Not only have these people been on my committee but I have had numerous classes with them and learned so much. In addition, I would like to thank Dr. Zhi-Jun Liu who always made time for my questions even though he was not on my committee. To all the other faculty and staff in the department of Geography at UNCG whom I have drawn so much from, thank you. Special thanks goes to Tammy Capps, a geographer and UNCG alumni, who provided me with the study site for my research. Her hospitality and accommodations for my research go unmatched.

I would also like to thank all my fellow students whom I have shared this experience with. Countless hours have been spent in the field with Ari Lukas,

Stacy Johnsonville, and Dr. Jacob Turner from which I have been left with the fondest of memories. I especially cannot thank Dr. Jacob Turner enough. He has helped me endlessly with my dissertation fieldwork and has been an incredible friend and pillar of support. My endless array of questions regarding fieldwork never went unanswered by him even when he was in the throes of his own research.

Finally, I would like to thank my family. First to my incredible wife who encouraged and guided me through a process that she had previously been through herself. Having that support system from someone so close to me proved to be invaluable. Countless hours of her time have been spent proof reading and improving my work, and for that I cannot thank her enough. Lastly, I would like to thank my parents who always believed in me and pushed me to believe in myself, and for that I am forever grateful.

TABLE OF CONTENTS

Page

LIST OF TABLES

Page

LIST OF FIGURES

Page

CHAPTER I
INTRODUCTION

Scale is a fundamental concept in the field of geography. It is at the heart of all geographic analysis, allowing the capture of data at specific levels of spatial or temporal size. As suggested by Mike Goodchild, 'Scale is perhaps the most important topic of Geographical Information Science' (Goodchild, 2001, p.10). This is evident in Remote Sensing where aerial imagery is bound by the size and resolution of the image and time at which it was taken (Avery and Berlin, 1992; Jensen, 2005). At that size and time, the imagery conveys certain information about the landscape. If an image was then taken at a higher resolution one would learn new information about finer details of the landscape. In other words, a series of imagery at varying levels of scale conveys far more information than one image at a fixed spatial and temporal scale.

A multi-scale approach allows analysis at multiple levels of scale, both spatial and/or temporal. This approach allows for a greater understanding of concepts, such as hillslope hydrology and the role it may play within a larger drainage basin (Knighton, 1998, p.56). It would be difficult to have a strong understanding of how a drainage basin functions without understanding what is happening at the hillslope scale and vice versa. With each increasingly higher

level of spatial and temporal resolution we are able to learn new information about the landscape (Avery and Berlin, 1992; Jensen, 2005). Today, we are on the cusp of a new revolution in data acquisition and processing using unmanned aerial systems (UASs) at low altitudes and structure from motion processing techniques (Colomina and Molina, 2014; Nex and Remondino, 2014; Toth and Grzegorz, 2016). Using a UAS, it is now possible to collect data at temporal and spatial resolutions that simply were not possible just a few years ago.

UASs bring an approach to temporal scale that is highly adjustable (Harwin and Lucieer, 2012; Shahbazi et al., 2014; Uysal et al., 2015). The UAS allows for imagery to be captured at virtually any time barring flight restrictions in the area. Additionally, with the relative ease and low cost required to fly a UAS, imagery could be captured on a multi-temporal scale. This is now becoming common in farming operations where UASs are used to obtain imagery several times during the crops growth season for plant health analysis (Xiang and Tian, 2011; Bendig et al., 2013 Rokhmana, 2015). Looking at multi-scale from a spatial stand point, the UAS allows the capture of highly detailed local imagery from a range of 400 feet above ground surface and lower. This could then be incorporated with lower resolution satellite imagery within a GIS environment providing a multi-scale level of spatial detail. While scale and multi-scale have an overarching theme in this dissertation, the goal will be to better understand how the UAS fits into this important topic in geography.

Remote sensing has been experiencing a technological revolution in data collection over the last decade. Using high resolution (1cm pixel size) images, it is possible to model real world objects in a digital environment with higher precision than previously possible. This is highly advantageous to people in the scientific community of any field requiring three-dimensional reconstruction of the environment. Laser scanners coupled with global positioning systems and total stations can produce highly accurate point clouds for use in modeling software. However, laser scanners, despite their increasing use throughout the past few decades, are outside the financial range and expertise of most researchers. Close-range photogrammetry, also known as VHR, is far less expensive and thanks to recent advances in the field of computer vision (CV) and UASs, more easily acquired and modeled.

'Very High Resolution' (VHR) is a term that has been used in some of the literature to refer to this type of close range photogrammetric data and will be used in this research to refer to it also (Turner et al. 2012). The VHR resolution of these data are typically sub-decimeter, placing it well ahead of most satellite and high altitude aerial imagery. Despite its high spatial resolution, VHR lacks essential metadata typically associated with imagery used in the photogrammetric processes, such as the camera parameters and image orientation (Colomina and Molina 2014; Nex and Remondino 2014). Without this metadata, the typical photogrammetric methods cannot be used. This dissertation will examine the creation of three-dimensional data models produced

from very high resolution remotely sensed data. More specifically, this research will focus on the use of low-cost solutions in collecting and processing photogrammetric data for use in creating three-dimensional scene models via close range ground and UASs imagery. The goal of this research is to gain a better understanding of the accuracy, resolution and point cloud density obtained in the collection, processing and modeling of this type of data.

While the use of mini UAVs for creating digital 3D models has gained a lot of attention in the last few years, a number of questions remain unanswered. This dissertation will attempt to answer the following questions:

Q1: Are these 3d models appropriate to be incorporated into a Multi-scale analysis?

Q2: How will topography impact RMS error results?

Q3: How replicable is the accuracy of the mapping products within a site?

Q4: How many ground control points are needed and at what number do they no longer improve accuracy?

Q5: How does image collection (altitude, flight path, target type) and processing (image type) affect model outcomes?

Q6: When comparing two UAS types with varying camera quality, do improved cameras change accuracy, resolution and model outcomes when using Structure from Motion (SfM)?

Q7: Can the accuracy fall within survey mapping standards?

Q8: Will this data collection process and generated digital models be appropriate for monitoring change at a sub decimeter scale?

Answering these questions can help bring into focus the hazy areas surrounding the use of UAS imagery, and other unstructured imagery, for 3D model creation and high resolution digital mapping. These questions are elaborated upon throughout this dissertation.

Remote sensing is the process of collecting data from a distance for observation, analysis and decision making. There are many methods which have been used for this collection process including air balloons, satellites, helicopters, aircraft, both manned and unmanned, and even birds (Jensen, 2005). These elevated platforms are equipped with various types of instruments which make it possible to collect data from a distance, and usually pertaining to features on the earth's surface. Cameras are the most commonly used devices, however radio detecting and ranging (RaDAR) and light detecting and ranging (LiDAR) are also frequently used for data acquisition, RaDAR and LiDAR are typically more expensive than the proposed methods to investigate in this research (Jensen, 2016).

Unmanned aerial vehicles (UAVs), also commonly known as drones, are becoming an increasingly popular way of collecting remotely sensed data. UASs have been used for remote sensing since the mid-20th century. This increased

use is mostly attributed to the military as well as a small number of visionaries capable of funding the high costs associated with UAS development and use (Colomina and Molina 2014; Nex and Remondino 2014). However, in 2004, the first published papers relating to UASs were presented at the International Society for Photogrammetry and Remote Sensing (ISPRS) congress (Everaerts et al. 2004; Fransaer et al. 2004; Turner et al. 2012; Westoby et al. 2012; Mancini et al. 2013; Colomina and Molina 2014; Uysal et al. 2015). Since then, the number of UAS-related articles have grown to the point that the international photogrammetric community has set up a biennial conference dedicated to UAS-related use called the UAV-g (Colomina and Molina 2014). The increase in use can be attributed in large part to reduced cost, miniaturization and advances in CV algorithms required to process unstructured UAV data (Colomina and Molina 2014; Nex and Remondino 2014).

Technological advancements over the last ten years have allowed the manufacturers of UASs to produce a lower cost aerial vehicle (AV) and accompanying operating system. The operating system consists of a ground control station and communications data link. The current UASs coming to market now are equipped with advanced aviation control software, global navigation satellite systems (GNSS) for autonomous flight and location information, and gimbal stabilization for use with digital cameras of varying types. In addition, camera advancements have allowed manufacturers the ability to

produce smaller optical systems which have aided in bolstering the popularity of UAS use (Nex and Remondino 2014).

Equally important is the contribution from the software development community, specifically CV programmers (Colomina and Molina 2014). The CV community has developed data processing algorithms that are capable of image feature matching at very high resolution. It is because of this specific contribution that the unstructured imagery being captured by low altitude UAVs can be rectified, referenced, mosaicked and modeled in a 3D point cloud (Turner et al. 2012; Mancini et al. 2013; Nex and Remondino 2014; Colomina and Molina 2014). While this is an impressive technological advancement, there are still open-ended questions about the imagery's level of accuracy. However, the future use of UASs across a wide range of fields, including geography, looks promising.

Typical photogrammetry is completed with calibrated cameras that have known parameters which are incorporated into processing algorithms allowing for rectification and georeferencing of the imagery (Avery and Berlin, 1992; Jensen, 2016). Most low-altitude mini (weighting between .55 lbs. and 55 lbs.) UAS imagery is unstructured, meaning that most of the reference data, such as camera orientation and geographic position, for typical processing of aerial imagery is missing or unknown (https://www.faa.gov/uas/faqs/). Within the last few years however, CV developers and the photogrammetry community have come together to develop software that can analyze and process the

unstructured data provided by mini UAS imagery (Snavely, 2008; Nex and Remondino 2014; Colomina and Molina 2014). This group of algorithms and workflow is known as Structure from Motion (SfM). The workflow for SfM incorporates a number of algorithms, some old, some new, and some simply tweaked or improved to do a new job. Some of the most important algorithms in the SfM workflow are Scale Invariant Feature Transformation (SIFT), Approximate Nearest Neighbor (ANN), Random Sample Consensus (RANSAC) and Bundle Adjustment (BA) (Snavely, 2008; Wu, 2013). There are variations on these, but these are the most widely used. Software developers are bundling these algorithms, or variations of these, into software that can automate a large part of the procedure of processing large numbers of unstructured images for mosaicking, georeferencing, point cloud and 3D model creation (Kersten and Lindstaedt 2012).

Progress has been made regarding the use of unstructured mini UAS imagery in geomatics applications, however many unknowns still exist. For instance, can accuracy be improved during various aspects of collecting and processing of the imagery? Do changes in topography call for different flight or collection parameters? What levels of accuracy can be expected under certain collection and processing conditions? Are these digital models repeatable within a range of accuracy making them suitable for monitoring change? This research answers these questions and provides clarity regarding accuracy in the use of mini UAS imagery in geographic and geomatics applications.

CHAPTER II
LITERATURE REVIEW

2.1 Flight Planning and Data Collection

Flight planning is a critical component of collecting mini UAS imagery for geodata acquisition (Colomina and Molina, 2014). Careful design and planning, taking into account dimensions such as speed, height, waypoints and pathing can lead to more productive and safer data acquisition (Mayr, 2011). In addition, weather plays a large role in UAS flight as wind gusts of just 18 knots have been shown to cause horizontal and vertical deviations of the aircraft of 10m and 5m, respectively (Mancini et al., 2013). This research focuses on using an automated flight routine where the UAV follows a path of waypoints programmed into the flight system using GNSS coordinates. In addition, test flights were performed using a manual technique in situations where it would be dangerous or impossible to rely on autonomous flight systems (i.e., when flying close to or underneath tree canopies).

The UAS camera can be used in manual mode or autonomous mode collecting images at timed intervals. This research has follow the general consensus in the literature of setting image capture at a set interval, generally between one to five seconds depending on UAV speed, allowing for a more

consistent collection of images (Harwin and Lucieer, 2012; Nex and Remondino 2014; Clapuyt et al., 2016). Care must be taken to ensure enough images, at the proper interval, are captured to facilitate the level of forward and side overlap required by the processing algorithms. This is important because it is in these overlapping portions of the images that the matching algorithm functions. Turner (2012) suggested using the maximum speed his camera was capable of, approximately 1Hz. Imagery was captured from takeoff to landing without stopping as the UAV flew though the path of assigned waypoints. Mancini et al. (2013) also used an automated approach snapping images at one per second while flying at 4m/s and an altitude of 40 m.

2.2 Image Processing: Feature Matching, Extraction and Structure from Motion

The use of UAS unstructured imagery to recreate complex scenes requires a more in-depth approach than typically needed or used in photogrammetry (Qin et al. 2013; Colomina and Molina 2014). This is because certain metadata about the imagery is unknown, such as the interior and exterior orientations of the camera and calibration details. Algorithms, such as Scale Invariant Feature Transform (SIFT), created in the field of CV, have proven to be well suited for accommodating this lack of metadata (Nex and Remondino 2014; Colomina and Molina 2014). The process of model creation uses several different specialized algorithms that each do a very specific task. The first step and algorithm in the process is SIFT (Lowe, 2004). SIFT is what is known as a feature extractor. SIFT is responsible for identifying features in imagery and

storing these features of various sizes in a database coupled with descriptor information about each feature or ‘blob’ as they are sometimes referred. The SIFT process can store up to 128 different descriptors for each feature. The algorithm performs this task across all images in the set creating thousands of individual features for each image. These features and their accompanying descriptors are then used for matching by other algorithms. SIFT is incredibly robust and generally unaffected by scale, orientation and noise within the images, making it ideal for use with unstructured imagery (Snavely, 2008).

Following SIFT is a matching procedure that is comprised of a set of algorithms designed to match key points from the features and descriptors stored in the database (Snavely, 2008). Accomplishing this is typically completed via an approximate nearest neighbor algorithm working between image pairs and within each descriptor space (Ayra et al., 1998). The process then uses a distance metric, such as Euclidean distance or ratio test, to accept or reject alleged matches (Snavely, 2008). Succeeding this, a process must then be implemented to determine inliers and outliers to further filter out features that simply do not help in creating correspondence between images. This is accomplished by the Random Sample Consensus (RANSAC) algorithm and can be viewed as an error checking procedure used to isolate and remove outliers that do not help to complete the reconstructed geometry (Fischler and Bolles, 1987).

Once general correspondence has been estimated within the collection of unstructured imagery, the next step is the creation of SfM. Estimating view points and recreating scene geometry is a classic problem in photogrammetry when dealing with image correspondence. Many years of research has been devoted to solving this problem with regard to structured imagery (Snavely, 2008). Recent research has started to focus on SfM from unstructured image collections. This can be attributed to the enormous amount of imagery stored within the internet and the projects attempting to build complete 3D models from these randomly posted images of locations. One example would be attempting to build a digital model of the Eiffel Tower just from tourist and other people's images uploaded to the internet. Virtually every major landmark in the world is well represented by digital images uploaded to the internet through various social media outlets. This has made for a rich environment for scene visualization research and the development of sophisticated algorithms to solve the recreation problem (Snavely, 2008).

Once feature matching and extraction is complete, the features can then be used by the SfM algorithm to solve for three dimensional aspects of the scene. SfM operates under the same basic principles as stereoscopic photogrammetry but follows a different approach. Basically, both SfM and stereoscopic methods resolve a 3D scene from a series of overlapping images. The key difference lies in the fact that SfM algorithmically solves for the key metadata needed by the photogrammetric technique such as camera position,

orientation and scene geometry. The features are analyzed over time to construct their three-dimensional positions and the motion at which the imagery was captured. This is how the name structure from motion or SfM was derived (Snavely, 2008; Wu, 2013).

SfM typically uses an incremental approach to solve the large optimization problem. There are however, several different approaches that can be applied, such as the global and hierarchal methods. In addressing the incremental approach, the process usually begins with what is known as seeding (Snavely, 2008). Multiple images, usually two or three, are typically used to reconstruct a reliable initial geometry which is then followed by a process known as bundle adjustment. Bundle adjustment is the process of minimizing the reprojection error through refinement of camera and point parameters and is applied as images or batches of images from the collection are added to the initial seed (Triggs et al., 2000).

In the global approach, the bundle adjustment is applied to the entire image correspondence set which is typically more efficient but can have mixed results in terms of model quality. The hierarchal approach is a divide and conquer method that breaks the task into many smaller units to solve independently and recursively merges the units back together, performing a bundle adjustment only when necessary (Clapuyt et al., 2016). Regardless of the method, the goal and final product from SfM is the creation of a sparse point

cloud. Once created, the sparse point cloud can then be used in the generation of a dense point cloud which is generally what is needed for highly detailed 3D digital models and mesh generation (Snavely, 2008).

Creating the dense point cloud is accomplished by using two algorithms known as Clustering View for Multi-view Stereo (CMVS) and Patch-based Multi-view Stereo (PMVS2) (Furukawa and Ponce, 2007). These algorithms are implemented using the output from the SfM workflow, which are the camera poses and the original overlapping images, as inputs. The CMVS breaks the sparse model and images into manageable clusters and the PMVS2 is used to reconstruct a significantly denser point cloud cluster by cluster. This dense point cloud can then be used in additional processes such as meshing, texturing and creation of UVs (assigning an object coordinate to a texture coordinate). The later processes mentioned above are used to make a more photorealistic model instead of simply a cloud of points derived from the PMVS2 process (Furukawa and Ponce, 2007; Snavely, 2008).

In UAS imagery, a large number of possible camera poses and object coordinates can be generated. These are then refined using non-linear least squares minimization arriving at the best possible statistical result. This process is known as bundle block adjustment. For this process to work effectively, many overlapping images from different vantage points are needed of the scene. While the exact overlap for the specific situation can be difficult to know, it is not

uncommon for the overlap to be as high as 80% forward and 80% side. This can translate into a large number of images as the area of interest increases. Mancini et al. (2013) collected 800 images using a one second interval at a study site only 200 meters' square. Of those images, 550 were selected for processing.

The level of accuracy for these 3D scene models produced from UAV imagery can vary depending on several factors. One factor is that mini UAVs are small and easily affected by wind. This introduces the same problems manned flight suffers from, such as pitch, yaw and roll, except at an amplified level due to the small size of the UAV. Additionally, the UAV camera is relatively low in relation to variations in topography and the movement can cause large perspective distortions similar to relief displacement effects but more exaggerated (Avery and Berlin, 1992; Jensen, 2005; Turner, 2012). Another factor for error to be introduced is in the altitude of the UAV. The GNSS system is typically navigation grade and will not be able to maintain positioning within a meter horizontally and vertically. While some UAVs incorporate a barometric altimeter, they are typically only accurate to within a meter (Turner, 2012). In addition, wide angle lens camera types, such as a Go-Pro, can require additional processing of the imagery to remove the panoramic distortion or fisheye. This introduces new errors in the process of correcting the imagery rendering a large portion of the edges useless.

The more processing the imagery requires, the more the algorithm has to decide where pixels should be in the scene. One way to aid in this process is by placing ground control points (GCP) within the area of interest. These GCPs can then be measured to survey accuracy using a differential GPS and or a total station (Turner et al. 2012, Mancini et al. 2013). The number of GCPs to be used seems to vary in the literature. However, it was noted by Turner, et al. (2012) that using 63 GCPs did not process the images more accurately than did the same imagery processed with 20 GCPs. This would lead one to assume that there must be a certain number of GCPs that at some point yield no additional accuracy.

2.3 Applicable Studies

Torres et al. (2014) integrated multiple geo-technologies to create 3D models for use in documenting of an archaeology site in Spain. They used photogrammetry, both aerial and terrestrial, and LiDAR to build a hybrid 3D model. This study showed the inherent flaws and abilities of both types of data collection methods, photogrammetry and LiDAR. UAVs were used for large area collection while ground cameras and LiDAR were used to spot fill areas that were shadowed or needed additional detail. The authors created a better final product by overcoming the deficiencies of each individual methodology. Model resolution for aerial photogrammetry, terrestrial photogrammetry and LiDAR were 5cm, 2cm and 5mm, respectively.

Uysal et al. (2015) used a UAV to create a Digital Elevation Model (DEM) across a 5-ha site. The study's objectives were to evaluate the performance of a low-cost method of DEM generation through photogrammetry. The UAV was used to capture 200 photos at 60 m altitude with a standard digital camera. 50 by 50 cm aluminum plates were used as ground control points and measured by Real-Time Kinematic (RTK) GNSS which arrived at an accuracy of 2.37 cm. Point cloud density was 450 per m^2 with a total of 26,025,883 points in the final point cloud. Root mean square (RMS) error was used for accuracy analysis between the generated DEM and 30 randomly sampled points measured by RTK GNSS in the study area. Minimum error was 0.81 cm and maximum error was 8.55 cm. The authors determined that this method could produce products usable in geomatic applications within small areas.

Turner et al. (2012) created an automated technique for generating georectified mosaics from UAV imagery. Point clouds were created from structure from motion and feature matching photogrammetric techniques applied to the UAV imagery. The point clouds were georeferenced using both direct and indirect methods. The direct method attempts to solve the georeferencing problem using estimated camera positions while the indirect relies on ground control points. Both methods were compared and accuracy was found to be 65-120 cm for the direct method and 10-15 cm for the indirect. The UAV used had a navigation grade GNSS unit which was used to attach GNSS position information to the imagery header file. An onboard barometric altimeter was used to obtain

height instead of the GNSS generated height due to the navigation grade's relatively poor ability to determine height.

Suwardhi et al. (2015) used photogrammetric techniques with a combination of UAV and terrestrial imagery to map the Borobudur Temple Site in Indonesia. The authors use images captured via terrestrial cameras and from cameras mounted on UAVs to produce 3D models, DEMs, orthomosaics and dense point clouds at sub decimeter accuracy. These were used to create a web based database for monitoring deterioration, preservation, spatial management and dissemination purposes. The Borobudur site is 1km x 1km and the temple itself is 121m square and 35m in height requiring several different approaches to capturing the imagery needed to produce the final digital products.

Two different types of UAVs were used by Suwardhi et al. (2015) to capture imagery at different altitudes and for different uses. A fixed-wing UAV was used to image the grounds, flying a set pattern back and forth over the entire site at a height of 280m, covering one square kilometer. The purpose of this flight was to generate the DEM and orthophoto of the temple and surrounding area with a final resolution of 5cm. A Hexa-copter was used to image the temple flying at a height of 20, 30, 35 and 50m. The hexacopter was used to photograph areas that would be extremely difficult to capture by ground mounted cameras due the height and layout of the temple. The resolution of the ortho and 3D models from the hexa-copter were 2cm and 1cm depending on the height flown and product

produced. Terrestrial imagery was used to capture high detailing of the structure walls and had a resolution of sub-cm. A geospatial database was used to store and relate the products created while a web application was developed for visualization.

Westoby et al. (2012) introduced SfM from a geomorphological perspective. High-resolution DEMs were created using the SfM technique and compared to terrestrial LiDAR of the same area. Decimeter-scale vertical accuracy was found to be achievable using the SfM approach to DEM creation. The site surveyed contained complex topography and a range of land-covers, resulting in a wide variety of imaging scenarios to challenge SfM. The authors found the use of SfM to be an effective and inexpensive method for capturing high-resolution data for small study areas. They also determined that each study area was different and may require a different approach when capturing imagery for use in the SfM process. It was found that extremely dense point clouds were achievable using SfM, even in the range of 10^3 points per m^2. Variation in cloud density is thought by the authors to be largely determined by the exposure of the imagery captured. In other words, the lightness or darkness of the image determines in large part, the clarity or texture of the terrain in the image which in turn affects the outcome of the densification algorithm. This would be significant dealing with the cameras mounted on lower cost UAVs as they tend to have fixed or limited exposure parameters determined by the f-stop and shutter speed.

Kersten and Lindstaedt (2012) investigated using photogrammetry for creating 3D models from free or low-cost software while noting how they compare in regards to accuracy, repeatability and reliability. Bundler/PMVS2, VisualSFM, Autodesk 123D Catch beta (now available out of beta) and Agisoft's PhotoScan were used in this study for creating the 3D models from images taken from standard cameras. The first two software packages, Bundler/PMVS2 and VisualSFM, are open source, completely free and available as downloads online. PhotoScan, while not free, is a low-cost software package costing around $180 U.S. dollars for the standard product. Autodesk 123D Catch beta is a web service, which is also free, but places limits on the number of images that can be used to source the model and allows less control over the model creation automating many of the choices available in the other three software packages. The software was tested on archaeological objects from several locations and then compared with data sets from terrestrial laser scanners and/or fringe projection systems. Kersten and Lindstaedt (2012) compared the SfM models to these two systems, terrestrial laser scanners and/or fringe projection systems, because they are considered the pinnacle of 3D model creation methods but are expensive and require a high level of expertise to use. An Obsidian carving, a stone statue, a ceramic pottery piece, a limestone architectural fragment and a carved dhow (boat) made from gypsum-lime plaster were all modeled using a variety of the methods mentioned above. For reasons not discussed by the authors, not all methods were used on each object. Kersten and Lindstaedt

(2012) found that the image based systems were able to create 3D surface models for archaeological applications with very similar quality to that of the more expensive TLS and/or structured light systems. Also, the authors stated that the image based systems were fast and easy to use while maintaining flexibility and cost-effectiveness. All that is required at the archaeology location is a camera and some form of scale bar. In one of the test examples, the imaged models of the moai statue were in the range of 1.3mm and 1.6mm of the TLS which are very promising results for archaeological use.

CHAPTER III
METHODS

3.1 Remote Pilot License

To fly a UAV for commercial or government use in the United States one must obtain a Remote Pilot's License from the Federal Aviation Administration (FAA). Additionally, each state can have its own rules and licensure supplemental to the FAA's. This is true for North Carolina which requires a UAV pilot to take a 'knowledge' test and obtain either a commercial or public use license depending on the pilot's affiliation. The FAA's Remote Pilot's License is by far the more rigorous of the tests and of course supersedes any individual state laws or requirements (https://www.faa.gov/uas/faqs/).

The FAA Remote Pilot law, 14 code of federal regulations (CFR) part 107 of the Federal Aviation Regulations, requires that any person seeking to become a UAS pilot flying in the United States take a special test at one of the FAA's certified testing centers. The test contains 60 plus questions and covers twelve specific topics listed in Table 1. The topics are designed to ensure a high level of understanding regarding flight and flight safety in the United States airspace. The UAS pilot not only has to understand topics specific to UASs but also topics

regarding manned flight. This is to ensure that the remote pilot does not interfere in anyway with manned flight while flying a UAS in the United States airspace.

Table 1. Remote Pilot – Small Unmanned Aircraft Systems Study Guide from FAA.

Applicable Regulations
Airspace Classification, Operating Requirements, and Flight Restrictions
Aviation Weather Sources
Effects of Weather on Small Unmanned Aircraft Performance
Small Unmanned Aircraft Loading
Emergency Procedures
Crew Resource Management
Radio Communication Procedures
Determining the Performance of Small Unmanned Aircraft
Physiological Factors (Including Drugs and Alcohol) Affecting Pilot Performance
Aeronautical Decision-Making and Judgment
Airport Operations
Maintenance and Preflight Inspection Procedures

The initial requirements, before August 2016, stated that only a certified pilot could fly a UAS in the United States airspace. It took the FAA years to review the rules and requirements to allow UASs in the United States airspace.

During this time the FAA simply determined that without final rules and regulations in place, the UAS pilot would have to be a licensed pilot. Initially, the researcher started to proceed down the path of becoming a certified pilot. During the summer of 2016 the researcher attended a two-week ground school as required by the FAA to prepare for the written exam.

Shortly after completing the ground school and while preparing for the FAA's pilot exam, the FAA adopted the long-awaited regulations for UAS flight in the United States airspace known as 14 CFR part 107 of the Federal Aviation Regulations. The researcher immediately signed up for the new UAS test at the Greensboro testing facility and began reviewing the newly released rules and regulations. In October of 2016, the researcher passed and received a temporary certificate which allowed the researcher to fly until the permanent license was received two months later. As part of the federal regulations, the UAV certificate holders must retake the exam every two years to keep the license active.

3.2 Aerial Targets

Ground control point (GCP) coordinates are required to accurately 24eoreferenced imagery from a UAS (Rosnell and Honkavaara, 2011; Harwin and Lucieer, 2012; Torres et al., 2014; Fernández-Hernandez et al., 2015; Clapuyt et al., 2016). In the study area, highly accurate survey equipment was used to determine cartesian coordinates of the GCPs. The GCPs were marked with plastic stakes driven into the ground at each location. A more in-depth

discussion of the process can be found in the ‘Ground Control’ section below. Aerial targets were carefully placed over the stakes, centering the middle of the target over the stake in the ground. During the UAV flight the targets on the ground are then captured in the aerial imagery. The targets are used to identify the GCP’s coordinates for processing by the SfM software. It is important that the targets are easily identified so that the center of the target can be pinpointed and marked within the SfM software. Target attributes such as size, shape and pattern can have an impact on the accuracy of the results (Harwin and Lucieer, 2012; Torres et al., 2014).

The targets for this study were made from a synthetic construction material similar to vinyl flooring. The material was purchased in 4 by 8-foot sheets and cut into roughly 2 by 2-foot squares. Each side of these 2 by 2-foot squares (Figure 1) was then painted with either an iron cross or checker pattern. A hole was then drilled through the center of the targets to allow an accurate placement of the target on the stake representing the GCP. Additionally, the targets are light weight, flexible and weather resistant making them suitable for a variety of conditions.

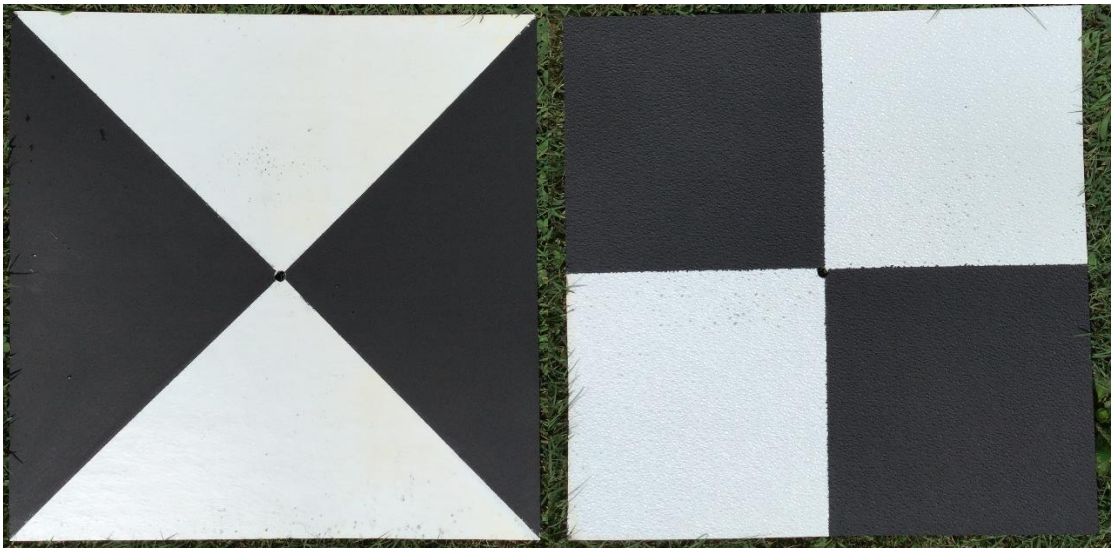

Figure 1. The Iron Cross and Checker Patterns, Respectively, Used on the Aerial Targets in This Study.

3.3 Study Area

The topography, vegetation and geology of the Earth is not homogeneous and mapping via UAS using standard imagery has been shown to be influenced by these factors (Avery and Berlin, 1992; Jensen, 2005; Turner et al. 2012). The project requirements for this was to locate a site that had variable elevation to test if accuracy was effected and the best method to minimize the distorting effects in the digital models being created by SfM. In addition, a site that was challenging and incorporated some sort of relief, vegetation, etc. rather than simply a level mowed field, would be advantageous for testing under situations that would normally be found in the Piedmont region.

The original proposal was to incorporate multiple sites in this study to test all the above-mentioned parameters. However, as researched progressed it became clear that this was not feasible for multiple reasons. First, obtaining permission to access multiple locations proved difficult as each site would require multiple visits during the research period. At times accessing a location could be under short notice or canceled requiring to be rescheduled as weather conditions needed to be optimal and consistent during the testing period. In addition, time in the field would require that the landowners vacate the site during the UAS activities in capturing imagery. Third, the test parameters required that ground control be left on site and not disturbed during the testing period. Fourth, the public perception of UAVs is often negative and many in the public fear laws could be broken and put them personally in jeopardy. Lastly, the process of surveying a two-hectare site, keeping the GCPs cleared of vegetation during the testing period, and requiring six to eight field days per site to gather the amount of data needed for testing is enormous and quickly proved impractical.

Fortunately, an alumnus of the UNCG geography department was sympathetic to the cause, owned a large tract of land, and was willing to help provide a site for this study. The site was the Native Son Vineyard located in the Uwharrie mountains within Franklinville, North Carolina (Figure 2). The site was a rural area comprised of rolling hills and farmland with the vineyard sitting atop of a hill. The site contained several buildings including a wine processing facility and cabin that was used as a staging area during the research. The entire farm is

roughly ten hectares with topographic relief and above ground features that created a unique challenge necessary to evaluate the suitability of terrain modeling by a UAS. Additionally, the vine growth over a full season allowed for the testing of this type of imagery for use in change detection and other monitoring type analyses. The vineyard itself consists of approximately two hectares of row vines and was bordered on three sides by forest. The terrain was south east sloping with undulating ground features (Figure 3). The grass was kept mowed to approximately 2-3 inches with bare earth in some areas.

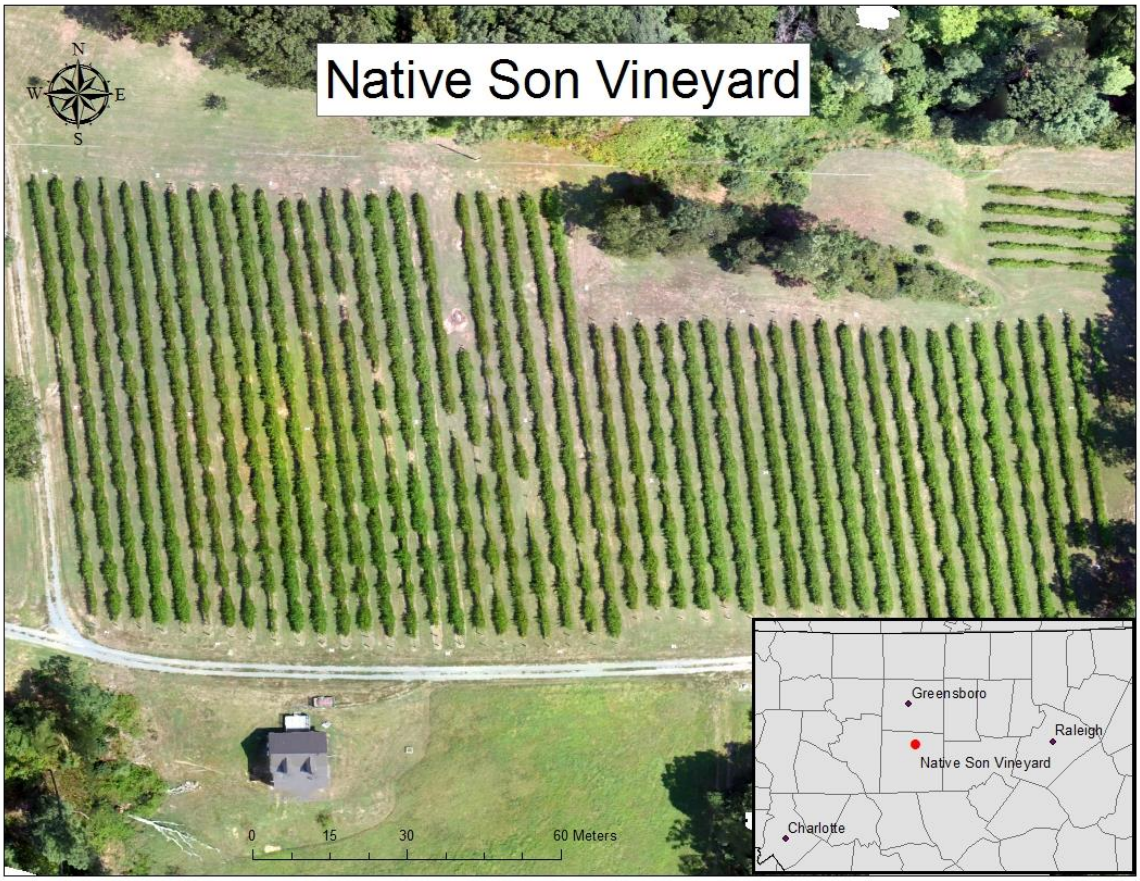

Figure 2. Native Son Vineyard Location Map.

Figure 3. Native Son Vineyard Topography.

3.4 Ground Control

Ground control points were established at the site using both GNSS and total station survey techniques. The first step in establishing ground control was to perform a rapid static GNSS survey on two locations within the vineyard. A planning survey was performed to establish the optimal time of day and point locations. Trimble® Planning software was used for this task which allowed for an obstruction survey, dilution of precision (DOP), sky plot, number of satellites and visibility in association with the most current almanac. The DOP and number of satellites analysis both showed optimum time frames for data collection to be in the 11:45pm - 3:30pm range. The two control points, named GPS1_NSV and GPS2_NSV, were collected at 11:51am – 12:36pm and 12:46pm – 1:31pm respectively and within the optimum collection time span. This was done using a TopCon® GR-3 survey grade GNSS receiver. Once data were collected for each

of the two control points it was uploaded to the National Geodetic Survey Online Positioning User System (OPUS) for calculation of the points' coordinates. The corrected OPUS solutions were then used as the starting point for the total station survey. Table 2 shows the corrected positional errors for GPS1_NSV and GPS2_NSV in NAD_83(2011) (EPOCH:2010.0000). OPUS report in Appendices.

Table 2. OPUS Correction Error for Both GPS Collections.

OPUS GPS Survey Point	LAT Error	LONG Error	EL HGT Error
GPS1_NSV	0.004(m)	0.003(m)	0.012(m)
GPS2_NSV	0.006(m)	0.002(m)	0.023(m)

Once the two control base points were established a grid system was laid out and ground control was expanded using a total station. Thirty-one ground control points were established from the original two GNSS coordinates using a Topcon® GTS-233W total station. The grid had to follow certain aspects of the terrain since the vine system on the site created obstructions making placement of ground control points difficult. It was determined that placing all points in the center of the walkways between vine rows (Figure 4) and at the end of the rows would provide the best visibility in leaf on and leaf off conditions. One consideration for ground control in this study was that the more points used increases cost and time. For this reason, it was determined, that while more points might be useful, it was beyond the scope and ability of this study.

Figure 4. View Obstruction from Vines.

The total station survey began by entering the points from the GNSS survey in the total station's data collector and setting the coordinate system. The total station was then set up on GPS1_NSV and backsighted to GPS2_NSV to orient the survey. Once this was accomplished the additional points in the grid were located using the sideshot method. To test the accuracy of the total station location a sideshot was repeated during the survey from different base points. This repeated sideshot confirmed the assumption that the expected error from the total station would be significantly below the level of error expected from the UAS mapping process. Table 3 shows the two points shot in at the same location from different base points in the North Carolina State Plane meters. Figure 5 shows the survey map.

Table 3. Sideshots from Diffferent Base Setups to the Same Ground Location.

Point	Northing (m)	Easting (m)	Elevation (m)	Description
8	229849.895	540825.631	272.769	GCP
8	229849.897	540825.617	272.768	GCP
8	0.002	0.014	0.001	Difference

Figure 5. Total Station and GPS Survey.

3.5 Hardware

Two UASs were used in this study, the DJI Phantom 3 Professional (P3P) and the DJI Phantom 4 Professional (P4P). The P3P was the UAS originally

purchased to be used in this research, however, during the field work the motherboard on the P3P suffered a catastrophic failure. A second UAS (the P4P) was then purchased to continue the research. The UASs have several different features that make them distinguishable from each other. Most important of these is the camera and shutter mechanism. Rolling shutters are typical of lower cost digital single-lens reflex (DSLR) cameras and present blurring issues when used by a moving UAS for image collection (Clapuyt et al. 2016; Kraft et al. 2016). This is the type found on the P3P. The P4P has a mechanical (global) shutter mechanism which exposes the sensor faster and more uniformly reducing the motion blur that accompanies the cameras fitted with rolling shutters. Additionally, the P4P's camera is 20-megapixels and the P3P is only 12.4-megapixels.

The P3P used in this study was a quadcopter made by DJI (Figure 6). The P3P is an electric, multirotor system. It was fitted with a gimbal mounted 12.4-megapixel DSLR camera with a Sony EXMOR 1/2.3" sensor and a maximum image size of 4000 x 3000 pixels. The batteries were 4480-mAh, 15.2 V lithium-polymer based with a flight time of approximately 24 minutes per battery. Additionally, the UAS is equipped with a barometric altimeter and a navigation grade GNSS receiver capable of using both the GPS and GLONASS systems. The P3P is capable of autonomous flight which can be programmed using flight planning software. In addition, the camera can be programmed to operate autonomously at timed intervals allowing for a more consistent image collection.

The UAV has a maximum flight time of 24 minutes; however, some flight control packages offer a ‘return for new battery’ function. This function saves the UAV’s last point in the flightpath allowing the UAV to return to the home point acquire a new battery and resume the mission. This function allows for much longer flight missions times than were previously possible in a low cost UAS (DJI, https://www.dji.com/phantom-3-pro/info).

Figure 6. DJI Phantom 3 Professional Quadcopter.

The P4P used in this study is a quadcopter made by DJI (Figure 7). The P4P is an electric, multirotor system. It is fitted with a gimbal mounted 19.96-megapixel digital single-lens reflex (DSLR) camera. It has a mechanical (global) shutter with a 1-inch complementary metal-oxide semiconductor (CMOS) sensor. The maximum image size of the camera is 5472 x 3648 pixels. The batteries are 5870-mAh, 15.2 V lithium-polymer based with a maximum flight time of approximately 30 minutes per battery. Additionally, the UAS is equipped with a

barometric altimeter and a navigation grade GNSS receiver capable of using both the GPS and GLONASS systems. The P4P is also capable of autonomous flight and image acquisition as seen above in the P3P. It also can be used with all the same aftermarket apps that allow a host of features not immediately available from the Manufacturer, such as the 'return for new battery' function previously mentioned (DJI, https://www.dji.com/phantom-4/info).

Figure 7. DJI Phantom 4 Professional Quadcopter.

3.6 Flight Planning

There are a multitude of rules, regulations and safety concerns when preparing to fly a mission in a given area. It is the responsibility of the pilot to understand and be aware of any of these that apply. While there are several websites and information portals pilots use to stay current on these topics it is difficult to know and check all of these. In response to this the FAA has

developed a mobile application to help unmanned aircraft operators know if there are any restrictions or requirements in the area they intend to fly. The app is called B4UFLY and can be downloaded from the FAA website (Figure 8). Once the app is activated, and permission is given for it to access your current location, it will immediately display a map and relevant information related to the proposal site. One of the most critical pieces of information the app displays is current flight restrictions. This would include such things as airport buffer zones, which are three to five-mile request permission zones, and temporary flight restrictions or TFRs. A TFR could be active in an area that for instance the president was visiting, firefighting or law enforcement activities were taking place, or surface-based hazards that could impact safety of flight were taking place.

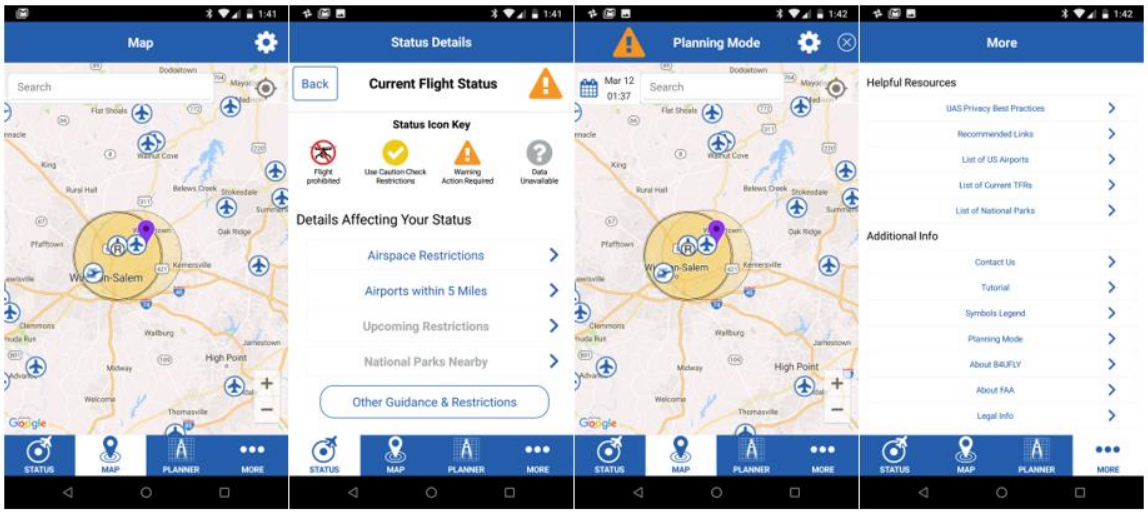

Figure 8. B4UFLY Mobile App Created by the FAA for UAS Operators.

Flight planning is crucial when collecting imagery for geomatics applications. This study used an app called Map Pilot by the company Drones Made Easy. The app is currently only available for the Apple™ operating system. It allows the user to plan many aspects of the flight mission in advance. Map Pilot allows the user to load something akin to Google Earth™ images where the user can then create polygon shapes as overlays to outline an area for the flight mission. Once the shape of the polygon is drawn on the screen, Map Pilot automatically draws the optimum flight path for the area (Figure 9). The user can then change from the default parameters to parameters of his or her choosing. Altitude, image type, image capture rate, side and forward overlap, speed and flight pattern can all be changed to match user needs.

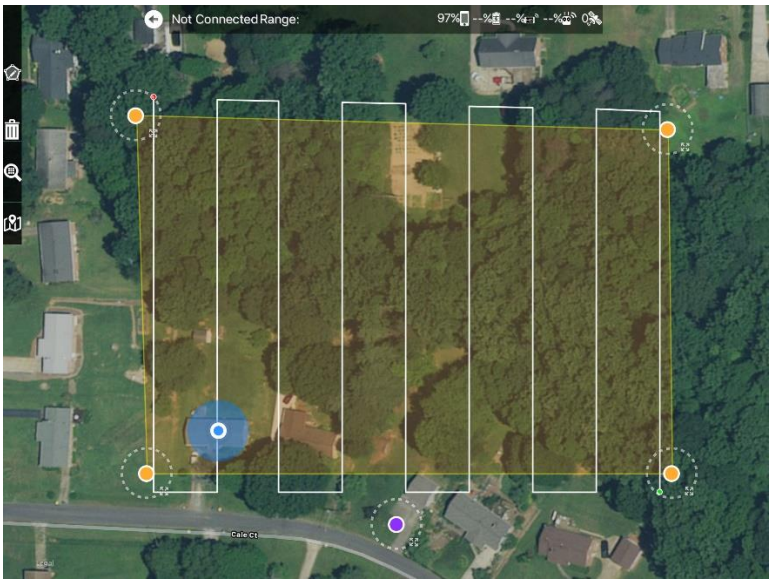

Figure 9. Map Pilot Flight Planning Software Area Selection and Flight Path.

Each mission plan was created in advance of the flight date and saved in the Map Pilot app. It was, however, necessary on several occasions to change, or add, a flight plan while in the field on the day of the flight. Figure 10 shows a screen shot from one of the missions stored in the app. A series of flights were undertaken on each of the seven field days at the Native Son Vineyard with more than 38 flights in total flown with successful data collection. Each flight type and specific parameters for the Native Son Vineyard can be seen in Table 4.

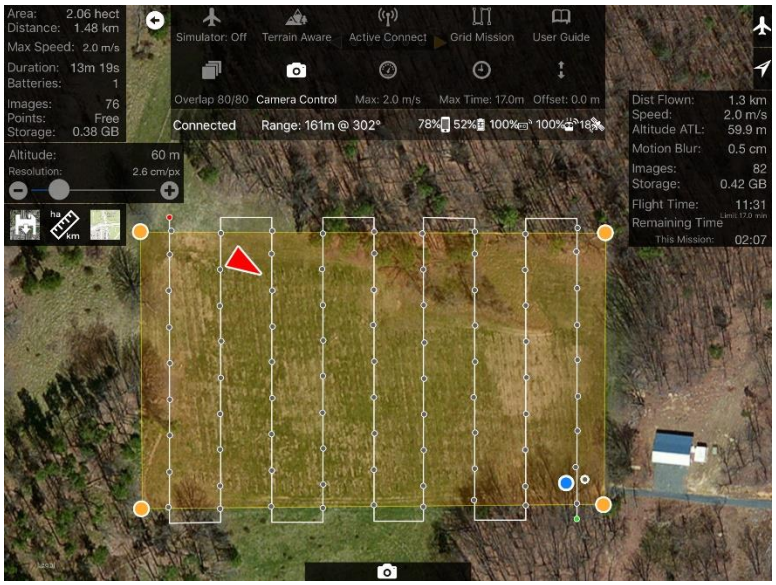

Figure 10. Saved Mission Results Screen from Map Pilot.

Table 4. All Flight Mission Types Flown at the Native Son Vineyard.

Flight Mission	Altitude	Overlap Fwd/Side	Image Type	Date	UAS Type	Mission
NSV_40_D1	40 m	80/80	Jpg	5/6/17	P3P	NSV_1
NSV_50_D1	50 m	80/80	Jpg	5/6/17	P3P	NSV_2
NSV_60_D1	60 m	80/80	Jpg	5/6/17	P3P	NSV_3
NSV_60_D1	60 m	80/80	RAW	5/6/17	P3P	NSV_4
NSV_80_D1	80 m	80/80	Jpg	5/6/17	P3P	NSV_5
NSV_40_D2	40 m	80/80	Jpg	5/7/17	P3P	NSV_6
NSV_50_D2	50 m	80/80	Jpg	5/7/17	P3P	NSV_7
NSV_60_D2	60 m	80/80	Jpg	5/7/17	P3P	NSV_8
NSV_80_D2	80 m	80/80	Jpg	5/7/17	P3P	NSV_9
NSV_40_D3	40 m	80/80	Canceled	7/23/17	P3P	NSV_10
NSV_50_D3	50 m	80/80	Canceled	7/23/17	P3P	NSV_11
NSV_60_D3	60 m	80/80	Jpg	7/23/17	P3P	NSV_12
NSV_80_D3	80 m	80/80	Jpg	7/23/17	P3P	NSV_13
NSV_40_D4	40 m	80/80	Jpg	8/6/17	P3P	NSV_14
NSV_50_D4	50 m	80/80	Jpg	8/6/17	P3P	NSV_15
NSV_60_D4	60 m	80/80	Jpg	8/6/17	P3P	NSV_16
NSV_80_D4	80 m	80/80	Jpg	8/6/17	P3P	NSV_17
NSV_60_D4_L	40 m	80/80	Jpg	8/6/17	P3P	NSV_18
NSV_80_D4_L	50 m	80/80	Jpg	8/6/17	P3P	NSV_19
NSV_60_D4	60 m	80/80	Jpg	8/6/17	P3P	NSV_20
NSV_40_D5	40 m	80/80	Jpg	9/10/17	P3P	NSV_21
NSV_50_D5	50 m	80/80	Jpg	9/10/17	P3P	NSV_22
NSV_60_D5	60 m	80/80	Jpg	9/10/17	P3P	NSV_23
NSV_80_D5	80 m	80/80	Jpg	9/10/17	P3P	NSV_24
NSV_60_D5_A	60 m	80/80	Jpg	9/10/17	P3P	NSV_25
NSV_60_D6_1	60 m	80/80	Jpg	11/15/17	P4P	NSV_26
NSV_60_D6_2	60 m	80/80	Jpg	11/15/17	P4P	NSV_27
NSV_60_D6_3	60 m	80/80	Jpg	11/15/17	P4P	NSV_28
NSV_60_D6_4	60 m	80/80	Jpg	11/15/17	P4P	NSV_29
NSV_60_D6_5	60 m	80/80	Jpg	11/15/17	P4P	NSV_30
NSV_60_D7_1	60 m	80/80	Jpg	11/29/17	P4P	NSV_31
NSV_60_D7_2	60 m	80/80	Jpg	11/29/17	P4P	NSV_32
NSV_60_D7_4	60 m	80/80	Jpg	11/29/17	P4P	NSV_33
NSV_60_D7_5	60 m	80/80	Jpg	11/29/17	P4P	NSV_34
NSV_80_D7_1	80 m	80/80	Jpg	11/29/17	P4P	NSV_35
NSV_80_D7_2	80 m	80/80	Jpg	11/29/17	P4P	NSV_36
NSV_80_D7_4	80 m	80/80	Jpg	11/29/17	P4P	NSV_37
NSV_80_D7_5	80 m	80/80	Jpg	11/29/17	P4P	NSV_38

3.7 Data Collection

The start of each data set collection began by setting up the aerial targets at each GCP location established with the total station. A total of thirty-one targets were laid out using a hole in the center of each target to align the target as accurately as possible over each plastic 9-inch tent stake driven into the ground. Once all targets were properly placed within the site the weather conditions were recorded to provide a reference for fluctuations in the final results. The flight mission plan was then selected, or if needed a new one created, within the flight planning application. The mission was then uploaded to the UAV and the flight started. Each flight was flown at 2 m/s and imagery captured at nadir.

During each flight, the Map Pilot application was monitored closely to check the real-time feedback on the flight parameters. Missed images and motion blur are important to check as they can quickly indicate whether the mission would need to be re-flown. This occurred on several occasions in which wind gusts or unexplained errors in the flight caused missed images and/or excess motion blur. Each of the first five flight days consisted of at least four standard flights at 40, 50, 60, and 80 meters above ground level (AGL) using the same flight path. This was done to keep a standard set of images across time. On days six and seven a different approach was taken and only the 60 and 80-meter flight altitudes were conducted. Instead of flying the 40 and 50-meter altitudes, additional flights were flown at the 60 and 80-meter altitudes removing

the targets from the study site manually by walking the site and collecting selected targets between flights. This was to test whether the additional targets left in the study area were affecting the accuracy outcomes by providing the SfM processing algorithm with additional tie points that would not have been available under reduced aerial target circumstances.

Once the standard mission set (40m, 50m, 60m, 80m) had been flown on days one though five, additional flights were flown to test for other influences affecting mapping accuracies. Flight path and target type were tested on day four with flights NSV_18, NSV_19, and NSV_20 (Table 4). All flights captured nadir photography only. On the third flight day it was not possible to complete the standard mission set due to changing weather conditions and flight numbers NSV 10 and NSV 11 were canceled (Table 4). Only two of the four standard mission flights, the 60m and 80m, were performed that afternoon.

3.8 Data Processing

Processing was completed using AgiSoft's® PhotoScan Professional. This software is very competitively priced and offers the user fine adjustment for those wanting more control over the processing parameters. They also offer an education discount package which allows the purchase of the professional version of the software at a reduced price. In addition, many of the software developers now offer monthly pricing, allowing for the short-term purchase of software for a fraction of the cost. The software becomes unusable once the time

period expires but can always be renewed at any time. This gives researchers the flexibility to lease these expensive products as their research agenda requires it.

Four levels of control scenarios were processed in PhotoScan Professional for each flight using the aerial targets in the study site to identify the locations of the thirty GCPs. The first control scenario implemented fifteen of the thirty ground survey points as control points with the other fifteen used as check points for accuracy assessment. The second control scenario used the fifteen check points from the first scenario as control, and the other fifteen GCPs used as control in the first scenario as check points. The third control scenario implemented eleven control points with the other nineteen used as check points. The fourth control scenario implemented eight control points with the other twenty-two used as check points. The standard mission set, and control scenarios were always processed using the same parameters for each step in the PhotoScan workflow.

Table 5. PhotoScan “Standard Mission” Alignment and Construction Processing Parameters.

Alignment parameters	**Values**
Accuracy	High
Generic preselection	Yes
Reference preselection	Yes
Key point limit	40,000
Tie point limit	10,000
Adaptive camera model fitting	Yes
Reconstruction parameters	
Quality	High
Depth filtering	Aggressive

The first step in processing each of the four control scenarios in the PhotoScan workflow was to align the images collected by the UAS. During this step, points within the image overlaps were matched, camera positions were estimated, and a sparse point cloud was created. Accuracy is typically always set to high in the PhotoScan alignment menu. This process only takes a few minutes and allows the user to see an estimate of all the camera positions for each of the images. This is an important initial phase as it allows one to identify areas where images may have been missed during flight.

Step two in the PhotoScan workflow involved locating the GCP targets and placing a marker on each photo. These were identified by locating the center points of the aerial targets in the images. Once a GCP for a specific location was marked, PhotoScan attempted to mark all other targets in the corresponding images. This process typically only gets close and usually requires the user to manually adjust each marker for greater accuracy. This can be time consuming when many targets and images are involved. For instance, in the 60-meter data set with thirty aerial targets, each target was found in a minimum of ten images and a maximum of twenty-eight images. This created a scenario in which the markers had to be manually adjusted 543 times in just one dataset. Figure 11 shows the marker adjustment process, which would take approximately 2-3 hours per data set. Once marker placement was completed, coordinates were imported from the total station/GNSS data files and camera locations were reoptimized.

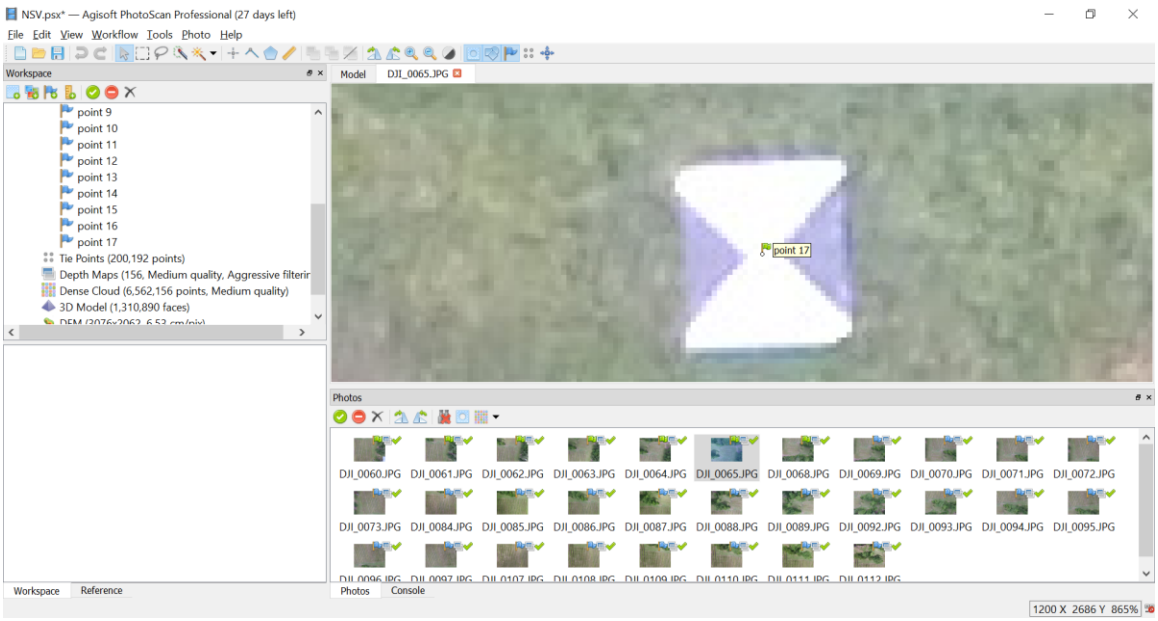

Figure 11. Marker Adjustment Process in PhotoScan Professional.

The third step involved generating the dense point cloud by densifying the sparse point cloud. This was the most computationally intensive and time-consuming step in the PhotoScan workflow. Each dense point cloud took several hours to complete. The DEM and Orthomosaic were then created using the dense point cloud. Finally, a PhotoScan report was generated for each standard flight and control scenario that recorded all processing parameters.

CHAPTER IV
RESULTS

These results were obtained based on seven days of flights at the Native Son Vineyard. The seven days spanned across the full growing season of the vineyard with the first flight taking place on May 6th, 2017 and the final flight on November 26th, 2017. Thirty-eight flights were performed at a range of different altitudes and under a variety of scenarios including different target types, flight paths, UASs, and levels of ground control.

While data for days one through five were collected at four different altitudes, the results and discussion will focus primarily on the 60-meter collects. This is due to several factors that presented themselves during the field work and data processing phases. First, the 60-meter flights provided the most consistent data set having been flown on every one of the flight days and included all the different flight scenarios mentioned above. Second, the 60-meter collected data provided higher accuracy (further detailed in the altitude comparison section) and reduced the processing times as compared to the 40 or the 50-meter data sets and was nearly equal in accuracy to the 80-meter. Third, the image resolution for the 60-meter was only slightly lower from the 40 and 50-meter data sets. Table 6 below shows the ground resolution for all four altitudes. Lastly, the 60-meter

flights were safer to fly using the automated flight control as it easily cleared all tree heights even as the UAS moved to the higher terrain at the west end of the vineyard. The 80-meter was equally accurate when compared to the 60-meter except for the lower ground resolution and lack of a complete data set.

Table 6. Comparison of Ground Resolution by Altitude.

Flight Altitude	Approximate Ground Resolution	Approximate Number of Images
40-meter	1.64 cm/pix	156
50-meter	2.06 cm/pix	110
60-meter	2.47 cm/pix	82
80-meter	3.42 cm/pix	52

Table 7 contains all of the 60-meter flights processed at four levels of control with their associated RMS error. The flight code is derived from the abbreviated name of the location, the altitude of the flight in meters, the day of the flight, the level of control, and any deviation from the standard flight parameters respectively. Flights from day 6 and day 7 were flown using the P4P UAS as the P3P suffered a motherboard failure and could not be repaired in time to be used on the final two flight days.

Table 7. All 60-Meter Flights with Their Associated RMS Errors.

Flight Code	Check	Control	X Err (cm)	Y Err (cm)	Z Err (cm)	Tot (cm)
NSV_60m_D1_2	15	15	1.715	2.110	2.505	3.697
NSV_60m_D1_3	15	15	3.553	1.986	1.990	4.531
NSV_60m_D1_4	19	11	2.154	1.843	1.825	3.372
NSV_60m_D1_5	22	8	2.475	1.677	2.162	3.690
NSV_60m_D2_2	15	15	1.774	2.132	1.529	3.168
NSV_60m_D2_3	15	15	4.148	1.964	1.414	4.802
NSV_60m_D2_4	19	11	2.181	1.839	1.141	3.073
NSV_60m_D2_5	22	8	3.271	1.650	1.529	3.970
NSV_60m_D3_2_LW	15	15	1.375	2.432	2.066	3.476
NSV_60m_D3_3_LW	15	15	1.352	2.281	2.606	3.719
NSV_60m_D3_4_LW	19	11	1.220	2.441	2.728	3.859
NSV_60m_D3_5_LW	22	8	1.817	2.443	3.264	4.464
NSV_60m_D4_2	15	15	1.859	2.081	2.642	3.843
NSV_60m_D4_3	15	15	3.946	2.071	2.267	5.001
NSV_60m_D4_4	19	11	2.040	1.802	2.556	3.734
NSV_60m_D4_5	22	8	2.875	1.671	2.691	4.279
NSV_60m2_D4_2_LW	15	15	1.233	1.421	1.913	2.685
NSV_60m2_D4_3_LW	15	15	1.812	2.127	3.137	4.202
NSV_60m2_D4_4_LW	19	11	1.642	1.921	2.944	3.880
NSV_60m2_D4_5_LW	22	8	1.477	1.309	2.548	3.223
NSV_60m3_D4_2_Tar	15	15	1.709	2.390	1.935	3.518
NSV_60m3_D4_3_Tar	15	15	3.797	1.910	1.699	4.578
NSV_60m3_D4_4_Tar	19	11	1.796	2.073	1.908	3.341
NSV_60m3_D4_5_Tar	22	8	2.377	1.755	2.364	3.784
NSV_60m_D5_2	15	15	1.919	2.012	2.681	3.863
NSV_60m_D5_3	15	15	4.075	1.880	2.221	5.007
NSV_60m_D5_4	19	11	1.981	1.700	2.405	3.550
NSV_60m_D5_5	22	8	2.578	1.582	2.205	3.744
NSV_60m2_D5_2_Ang	15	15	1.655	1.899	2.388	3.471
NSV_60m2_D5_3_Ang	15	15	2.407	1.960	1.864	3.621
NSV_60m2_D5_4_Ang	19	11	1.761	1.651	2.985	3.839
NSV_60m2_D5_5_Ang	22	8	2.164	1.594	4.390	5.147
NSV_60m_D6_2	15	15	1.182	2.084	1.291	2.722
NSV_60m_D6_3	15	15	1.313	1.934	1.308	2.679
NSV_60m_D6_4	19	11	1.022	1.874	1.513	2.617
NSV_60m_D6_5	22	8	1.206	1.853	1.206	2.519
NSV_60m_D6_6	24	6	1.219	1.922	1.518	2.736

NSV_60m_D6_7	25	5	1.230	1.985	1.907	3.015
NSV_60m_D6_8	26	4	1.017	3.151	1.938	3.837
NSV_60m_D6_9	27	3	2.217	2.917	6.559	7.513
NSV_60m_D7_2	15	15	1.268	1.873	1.463	2.694
NSV_60m_D7_3	15	15	1.070	1.633	1.646	2.554
NSV_60m_D7_4	19	11	1.065	1.704	1.517	2.519
NSV_60m_D7_5	22	8	1.249	1.675	1.507	2.577

4.1 PhotoScan Accuracy

The accuracy measurements from PhotoScan's report have been visually crosschecked using a shapefile made from the survey data coupled with the PhotoScan generated orthomosaics within ESRI™ ArcGIS® Pro. Six points, three control and three check, were selected across the vineyard from NSV_60m_D5_5_no20 to be crosschecked. The PhotoScan reports are generated at site level scale and thus the ellipses are amplified so that they can be seen more easily. This allows for easy visualization and quick comparison of survey points across the site. The direction and exaggeration of the ellipse shows the trajectory and amount of error at each point relative to the other points. These error maps are not intended to show exact error values; however, the exact error values are provided in a table below the maps in the PhotoScan reports.

Figure 12 and Table 8 show one of the three check point comparisons using GCP nine. GCP nine had one of the largest errors in the flight data set used for crosschecking. The survey shapefile was overlaid onto the PhotoScan generated orthomosaic and digital elevation model (DEM). The distance between the point in the survey shapefile and its location in the orthomosaic was then

measured for each of the x, y and z coordinates. The same point was then compared to the PhotoScan report (Table 8). Figure 12 shows that the trajectory of error from the PhotoScan report closely matches the trajectory of error seen in the ArcGIS® Pro comparison. The greatest difference between the ArcGIS® Pro measurement and PhotoScan report error was in the z coordinate with a discrepancy of 4.5 cm. The X and y values were much closer at 2.3 and 1.1 cm, respectively.

Figure 12. Error Trajectory from Survey Point Nine in ArcGIS Pro Compared to PhotoScan Report, Respectively.

Table 8. Check Point Nine in the Orthomosaic Compared to Check Point Nine in the PhotoScan Report from 60m Altitude.

Point	X	Y	Z
Ortho 9	540789.715	229851.682	276.558
Survey 9	540789.624	229851.722	276.630
Difference (m)	0.090	-0.040	-0.072
Converted (cm)	9.020	-4.016	-7.210
PhotoScan Report (cm)	6.676	-2.873	-2.748
Discrepancy (cm)	**2.344**	**1.143**	**4.462**
NAD_1983_2011_StatePlane_North_Carolina_FIPS_3200			

Figure 13 and Table 9 show one of the three control point comparisons using survey point seventeen. Again, the survey shapefile was overlaid onto the PhotoScan generated orthomosaic and DEM. The distance between the point in the survey shapefile and its location in the orthomosaic is then measured for each of the x, y and z coordinates. The same point was then compared to the PhotoScan report (Figure 13). The trajectory for point seventeen in the orthomosaic is slightly different from the PhotoScan report. The trajectory of the x and y positioning is slightly more to the northwest where in the PhotoScan report it appears to only show error to the north. However, the error is so small for this location that it is difficult to discern the ellipse elongation (Figure 13). The greatest difference between the ArcGIS Pro measurement and PhotoScan report error was in the x coordinate with a discrepancy of 2.2 cm (Table 9). The y and z values were much closer at 1.3 and 0.7 cm, respectively (Table 9).

Figure 13. Survey Point Seventeen in ArcGIS Pro Compared to PhotoScan Report.

Table 9. Control Point Nine in the Orthomosaic Compared to Check Point Nine in the PhotoScan Report.

Point	X	Y	Z
Ortho 17	540913.137	229869.119	263.399
Survey 17	540913.114	229869.136	263.413
Difference (m)	0.022	-0.017	-0.014
Converted (cm)	2.255	-1.725	-1.433
PhotoScan Report (cm)	-0.006	-0.417	-0.640
Discrepancy (cm)	**2.261**	**1.308**	**0.793**
NAD_1983_2011_StatePlane_North_Carolina_FIPS_3200			

4.2 Altitude Comparison

The altitude comparison was accomplished using the data from day 2 and processed with eight control points and twenty-three check points. Unexpectedly, the overall accuracy improved with each increase in altitude (Table 10) with the highest RMS error at 7.43595 cm for the 40-meter data set. The lowest RMS error was found to be in the 80-meter data set at 4.86006 cm. The largest single

point error value recorded for each altitude (Table 11) revealed that the largest error of 13.865 cm was recorded at the 40-meter altitude for the Z parameter. The smallest maximum error of 3.26607 was recorded at the 60-meter altitude for the Y parameter. The Y parameter tended to have the lowest RMS error and the smallest maximum error for all flights at the vineyard.

Table 10. Day Two Flights at Four Different Altitudes with RMS Error in Centimeters.

Flight Code	Check	Control	X error (cm)	Y error (cm)	Z error (cm)	Total (cm)
NSV_40m_D2_5	23	8	4.37529	1.90536	5.70262	7.43595
NSV_50m_D2_5	23	8	5.45435	1.74638	4.18068	7.09069
NSV_60m_D2_5	23	8	4.80867	1.71368	2.50629	5.68696
NSV_80m_D2_5	23	8	3.32043	1.56662	3.18444	4.86006

Table 11. Maximum Error Value Recorded for Each Flight for X, Y, and Z.

Flight Code	Check	Control	X error (cm)	Y error (cm)	Z error (cm)
NSV_40m_D2_5	23	8	10.1655	5.1855	13.865
NSV_50m_D2_5	23	8	11.6481	3.90969	9.30742
NSV_60m_D2_5	23	8	11.2562	3.26607	4.98803
NSV_80m_D2_5	23	8	9.25169	5.08121	7.11106

All UAV flights have a level of natural variability due to the many factors that affect the flight of the UAV and image capture. Additionally, processing the flight data in PhotoScan has variability due to the objective nature of manually placing the markers to represent the survey points in every image. T-tests were used to help discern whether the variance in error between the flight altitudes was due to actual differences in the methods or simply due to natural variation in the data collection and processing. Twelve paired t-tests were performed at the

95% confidence interval for all combinations of the four altitudes tested and are summarized in Table 12. A full t-test example can be seen in Table 13. The null and alternative hypotheses used in all altitude comparison t-tests can be seen below.

$$H_0 : \mu_d = 0$$

$$H_1 : \mu_d \neq 0 \text{ (two-tailed)}$$

Table 12. Summary of All Twelve Paired Two Sample for Means T-Tests for the Altitude Comparison Data with Significant Comparisons in Bold.

Elevation Data Sets Compared		P(T<=t) two-tail	t Stat	t Critical two-tail
40_Total(cm)	*80_Total(cm)*	**0.00020442**	4.44305192	2.073873068
50_Total(cm)	*80_Total(cm)*	**0.00006949**	4.885834037	2.073873068
60_Total(cm)	*80_Total(cm)*	0.05437133	2.032280987	2.073873068
40_Total(cm)	*60_Total(cm)*	**0.00136613**	3.663276063	2.073873068
50_Total(cm)	*60_Total(cm)*	**0.00001832**	5.439197947	2.073873068
80_Total(cm)	*60_Total(cm)*	0.05437133	-2.032280987	2.073873068
40_Total(cm)	*50_Total(cm)*	0.54291292	0.618011959	2.073873068
60_Total(cm)	*50_Total(cm)*	**0.00001832**	-5.439197947	2.073873068
80_Total(cm)	*50_Total(cm)*	**0.00006949**	-4.885834037	2.073873068
50_Total(cm)	*40_Total(cm)*	0.54291292	-0.618011959	2.073873068
60_Total(cm)	*40_Total(cm)*	**0.00136613**	-3.663276063	2.073873068
80_Total(cm)	*40_Total(cm)*	**0.00020442**	-4.44305192	2.073873068

Table 13. Paired Two Sample for Means T-Test Results for 40-Meter to 80-Meter Comparison.

t-Test: Paired Two Sample for Means	*40_Total(cm)*	*80_Total(cm)*
Mean	6.4291	4.3067
Variance	14.5951	5.3028
Observations	23	23
Pearson Correlation	0.8326	
Hypothesized Mean Difference	0	
df	22	
t Stat	4.4431	
P(T<=t) one-tail	0.0001	
t Critical one-tail	1.7171	
P(T<=t) two-tail	**0.0002**	
t Critical two-tail	2.0739	

Statistically significant differences were present when the 40-meter data set was compared to both the 60-meter and 80-meter data sets with p-values of .0013 and .0002 respectively. Thus, the null hypothesis was rejected in both of those scenarios. No significant statistical difference was found when the 40-meter data set was compared to the 50-meter data set with a p-value of 0.5429. The null hypothesis was accepted for that scenario.

The 50-meter data set did show a significant statistical difference when compared to the 60-meter and the 80-meter data sets with p-values of .00001 and .00006 respectively. The null hypothesis was thus rejected in both of those scenarios. There was no statistically significant difference when the 60-meter data set was compared to the 80-meter data set with a p-value of .0543 and the null hypothesis was accepted in that scenario.

4.3 Ground Control and Accuracy

In order to determine the point at which additional ground control no longer improved accuracy, control points were systematically decreased and switched to check points during processing. This was accomplished by decreasing the number of control points from fifteen to eleven and then from eleven to eight. This resulted in three different control level scenarios. One additional scenario was added to this where the fifteen control points used in the fifteen-control scenario were swapped with the fifteen check points. The purpose was to determine if using the same number of targets but in different locations had an impact on accuracy. All control scenarios, with the associated survey points, can be seen in Table 14. Paired and unpaired t-tests were used to determine statistical significance at the 95% confidence interval between control scenarios. Unpaired t-tests were used when the check points were different between the comparisons.

$$H_0 : \mu_d = 0$$

$$H_1 : \mu_d \neq 0 \text{ (two-tailed)}$$

Table 14. Control Scenarios and Associated Survey Points Used.

15-Control Scenario	15-Control Scenario	11-Control Scenario	8-Control Scenario
Point 1	Point 3	Point 2	Point 2
Point 2	Point 4	Point 4	Point 5
Point 5	Point 6	Point 9	Point 7
Point 8	Point 7	Point 12	Point 11
Point 9	Point 11	Point 15	Point 17
Point 10	Point 13	Point 17	Point 18
Point 12	Point 14	Point 18	Point 25
Point 15	Point 16	Point 23	Point 30
Point 17	Point 19	Point 26	
Point 18	Point 21	Point 27	
Point 22	Point 23	Point 30	
Point 24	Point 26		
Point 25	Point 27		
Point 28	Point 29		
Point 30	Point 31		

In all control level scenarios for day one, none showed a statistically significant change in accuracy when using a paired or unpaired two sample t-test at the 95% confidence interval. The greatest difference was expected to be between the fifteen-control point and eight-control point scenarios. However, as can be seen in Table 15, the total accuracy outcomes are nearly identical at 3.69724 cm and 3.69039 cm for the fifteen-control and eight-control point scenarios, respectively. The largest variance in the control scenarios tested came from switching the control and check points under the fifteen-control point scenarios which switched control points from the corners of the study site to control points more centrally located.

Table 15. Day One Control Point Scenarios and Accuracy Outcomes.

Flight Code	Check	Control	X Err (cm)	Y Err (cm)	Z Err (cm)	Tot (cm)
NSV_60m_D1_2	15	15	1.7150	2.110	2.505	3.697
NSV_60m_D1_3	15	15	3.553	1.986	1.990	4.531
NSV_60m_D1_4	19	11	2.154	1.843	1.825	3.372
NSV_60m_D1_5	22	8	2.475	1.677	2.162	3.690

The comparison between the fifteen-control and eight-control scenario data sets (Table 16) from day two did prove significant using a paired two sample t-test at the 95% confidence interval yielding a p-value of 0.0174. However, none of the other control scenarios showed a statistically significant change in accuracy when using a paired or unpaired two sample t-test at the 95% confidence interval. Again, the largest variance in the control scenarios tested came from switching the control and check points under the fifteen-control point scenarios, though it still did not test significant using an unpaired two sample t-test.

Table 16. Day Two Control Point Scenarios and Accuracy Outcomes.

Flight Code	Check	Control	X Err (cm)	Y Err (cm)	Z Err (cm)	Tot (cm)
NSV_60m_D2_2	15	15	1.774	2.132	1.529	3.168
NSV_60m_D2_3	15	15	4.148	1.964	1.414	4.802
NSV_60m_D2_4	19	11	2.181	1.839	1.141	3.073
NSV_60m_D2_5	22	8	3.271	1.650	1.529	3.970

Unlike days one and two, which used the widthwise flight pattern, day three used the lengthwise flight pattern. The paired two sample t-tests run on the data from day three (Table 17) tested significant at the 95% confidence interval

when the fifteen-control scenario was compared to the eleven-control scenario and when the fifteen-control scenario was compared to the 8-control scenario. The p-value for the fifteen-control to eleven-control comparison was 0.015 and the p-value for the fifteen-control to eight-control comparison was 0.005. The variance for switching the control and check points under the fifteen-control point scenarios for day three this time showed the least variance of all the day three comparisons. This differed from the comparison outcomes from days one and two in which it showed the largest variance.

Table 17. Day Three Control Point Scenarios and Accuracy Outcomes.

Flight Code	Check	Control	X Err (cm)	Y Err (cm)	Z Err (cm)	Tot (cm)
NSV_60m_D3_2_L	15	15	1.375	2.432	2.066	3.476
NSV_60m_D3_3_L	15	15	1.352	2.281	2.606	3.719
NSV_60m_D3_4_L	19	11	1.220	2.441	2.728	3.859
NSV_60m_D3_5_L	22	8	1.817	2.443	3.264	4.464

The error rates (Table 18) from day four were slightly higher than any of the seven flight days at the 60-meter altitude. The data comparisons from day four did not prove significant using paired two sample t-tests at the 95% confidence interval. However, the comparison between the fifteen-control scenario to the eleven and eight-control scenarios proved significant at the 90% confidence interval level using the paired two sample t-test. The error rates and variance were greatest when switching the control and check points under the two fifteen-control point scenarios for day four. The comparison between these

two data sets however did not prove significant using the unpaired two sample t-test.

Table 18. Day Four Control Point Scenarios and Accuracy Outcomes.

Flight Code	Check	Control	X Err (cm)	Y Err (cm)	Z Err (cm)	Tot (cm)
NSV_60m_D4_2	15	15	1.859	2.081	2.642	3.843
NSV_60m_D4_3	15	15	3.946	2.071	2.267	5.001
NSV_60m_D4_4	19	11	2.040	1.802	2.556	3.734
NSV_60m_D4_5	22	8	2.875	1.671	2.691	4.279

Day five had the second highest error rates (Table 19) out of the seven flight days at the 60-meter altitude. None of the comparisons to the fifteen-control scenario proved significant at 90% or 95% confidence interval using the paired or unpaired t-test on this day. The error rates and variance were greatest when switching the control and check points under the two fifteen-control point scenarios for day five. The comparison between these two data sets however, again did not prove significant using the unpaired two sample t-test.

Table 19. Day Five Control Point Scenarios and Accuracy Outcomes.

Flight Code	Check	Control	X Err (cm)	Y Err (cm)	Z Err (cm)	Tot (cm)
NSV_60m_D5_2	15	15	1.919	2.012	2.681	3.863
NSV_60m_D5_3	15	15	4.075	1.880	2.221	5.007
NSV_60m_D5_4	19	11	1.981	1.700	2.405	3.550
NSV_60m_D5_5	22	8	2.578	1.582	2.205	3.744

Day six was flown, and data collected, using the new P4P UAS utilizing the improved camera and global shutter system. Also, this was the only data, from any of the flight days, that was processed under four additional reduced control scenarios dropping the number of control points to six, five, four and three. The variance and error rates (Table 20) from day six were the second lowest of all the seven flight days. Only day seven had lower variance and accuracy outcomes.

None of the day six comparisons to the fifteen-control scenario proved significant until the control was reduced to only four points. The 4-control point scenario, which hadn't been used on any of the other flight data, showed significance at the 90% confidence interval. Once the control was reduced to three, it showed significance at the 95% confidence interval. Switching the control and check points under the two fifteen-control point scenarios for day six resulted in improved accuracy. The improved accuracy for the control and check point switch was unique to only the day six and day seven data sets as all other switching control and check point scenarios resulted in reduced accuracy.

However, there was no statistical significance at either the five or ten percent level.

Table 20. Day Six Control Point Scenarios and Accuracy Outcomes.

Flight Code	Check	Control	X Err (cm)	Y Err (cm)	Z Err (cm)	Tot (cm)
NSV_60m_D6_2	15	15	1.182	2.084	1.291	2.722
NSV_60m_D6_3	15	15	1.313	1.934	1.308	2.679
NSV_60m_D6_4	19	11	1.022	1.874	1.513	2.617
NSV_60m_D6_5	22	8	1.206	1.853	1.206	2.519
NSV_60m_D6_6	24	6	1.219	1.922	1.518	2.736
NSV_60m_D6_7	25	5	1.230	1.985	1.907	3.015
NSV_60m_D6_8	26	4	1.017	3.151	1.938	3.837
NSV_60m_D6_9	27	3	2.217	2.917	6.559	7.513

Day seven variance and error rates (Table 21) were the lowest of all the seven flight days. Like day six, day seven also used the new P4P UAS utilizing the improved camera and global shutter system. None of the comparisons to the fifteen-control scenario proved significant at the 90% or 95% confidence interval using the paired or unpaired t-test on day seven. Switching the control and check points under the two fifteen-control point scenarios for days seven resulted in improved accuracy. However, there was no statistical significance at either the 90% or 95% confidence interval.

Table 21. Day Seven Control Point Scenarios and Accuracy Outcomes.

Flight Code	Check	Control	X Err (cm)	Y Err (cm)	Z Err (cm)	Tot (cm)
NSV_60m_D7_2	15	15	1.268	1.873	1.463	2.694
NSV_60m_D7_3	15	15	1.070	1.633	1.646	2.554
NSV_60m_D7_4	19	11	1.065	1.704	1.517	2.519
NSV_60m_D7_5	22	8	1.249	1.675	1.507	2.577

4.4 60m Collects Using Eight Control Points and Replicability of Accuracy

Table 22 contains the RMS error for all seven days of flights at the 60-meter altitude and using eight control points to 65eoreferenced the point clouds and orthomosaics. It is important to note that day six and seven were flown using the P4P UAS with the improved camera. Using the P4P UAS, also provided the lowest error of all seven days of flights at 60-meters. The day with the highest RMS error was day three, however, the 60-meter flight from that day was flown using the ‘lengthwise’ alternate flight pattern. This was the only day that the standard widthwise flight pattern wasn’t used due to time constraints on that date. However, as will be seen in the ‘Flight path’ analysis, the accuracy outcome difference between the widthwise and lengthwise flight paths were negligible.

Table 22. RMS Error for 60-Meter Data Collects Using Eight Control Points Across All Seven Flight Days.

Day	UAS	X error (cm)	Y error (cm)	Z error (cm)	Total (cm)
1	P3P	2.475	1.677	2.162	3.690
2	P3P	3.271	1.650	1.529	3.970
3	P3P	1.817	2.443	3.264	4.464
4	P3P	2.875	1.671	2.691	4.279
5	P3P	2.578	1.582	2.205	3.744
6	P4P	1.206	1.853	1.206	2.519
7	P4P	1.249	1.675	1.507	2.577

The two different UAS types showed only a small amount variability in the variance of total RMS error. The standard deviation for all 60-meter flights under the eight-control point scenario and across all seven flight days, including both UAS types, was 0.7159 (Table 23). The P4P had a lower standard deviation than the P3P with 0.0286 and 0.3003, respectively (Table 23). However, it is important to note that the standard deviation for the P3P was calculated from five flights while the standard deviation for the P4P used only two flights. The variability might have increased for the P4P if a larger data set was used.

Table 23. Standard Deviation and Variance of RMS Error Across All Seven Days and for Each UAS Type.

Statistic	X error (cm)	Y error (cm)	Z error (cm)	Total (cm)
Both UAS				
Var.	0.5512	0.0763	0.4561	0.5125
Sta. Dev.	0.7424	0.2762	0.6753	**0.7159**
P4P only				
Var.	0.0005	0.0080	0.0226	0.0008
Sta. Dev.	0.0216	0.0893	0.1504	**0.0286**
P3P only				
Var.	0.2311	0.1031	0.3359	0.0902
Sta. Dev.	0.4807	0.3211	0.5795	**0.3004**

The variance from the mean, across all seven days, was greater in the x and z coordinates than in the y coordinate (Table 23). However, once the data were separated into UAS types, the outcomes were different. The P3P data showed the same pattern of standard deviation distribution as the combined seven days of data in the x, y, and z coordinates. The x and z coordinates showed the highest variance and the y coordinate displayed the lowest in the P3P data. The P4P data resulted in a different outcome distribution with the x coordinate showing the least variance followed by the y and z coordinates respectively. In both the combined and isolated UAS data sets, the z coordinate always displayed the largest variance from the mean.

Figure 14 shows the total accumulated error at each check point across all seven days at 60-meters and under the eight-control point scenario. Points nine and thirty-one had the highest accumulated errors of any of the check points (Figure 15). The largest errors were found at the western end of the vineyard.

This was the highest elevation in the vineyard with the bare ground elevation 12 meters higher on the west end then the east end. Points nine and thirty-one had as much as four times the error of some of the other check points and were located only seventeen meters apart. Check point twenty-six had the third highest error and was located ten meters west of the center of the 167-meter-long vineyard. Points one and six were the two points with the lowest accumulated errors were located along the south edge of the vineyard. Point one is located in the western area and point six in the eastern area.

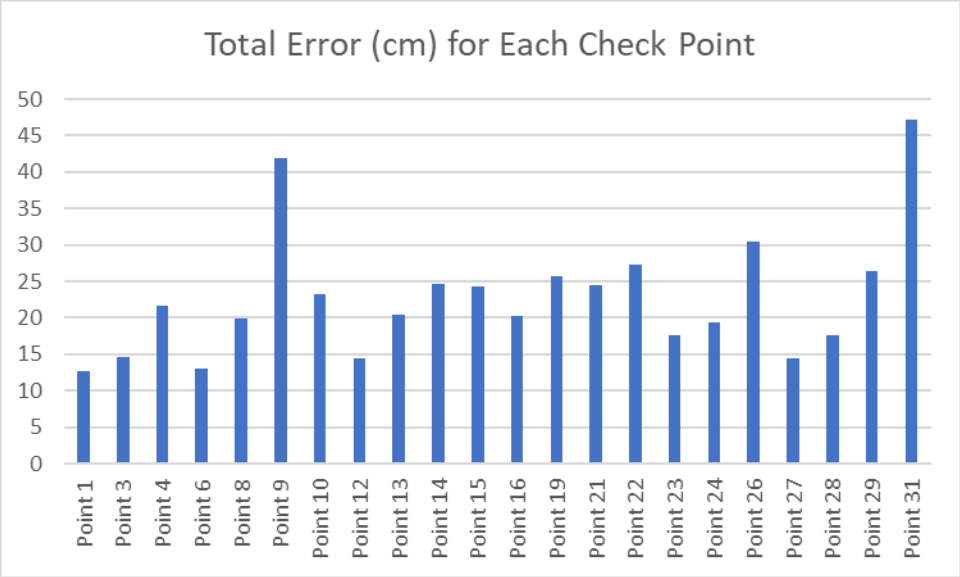

Figure 14. Total Accumulated Error for Each Check Point Across All Days Using Eight Control Points.

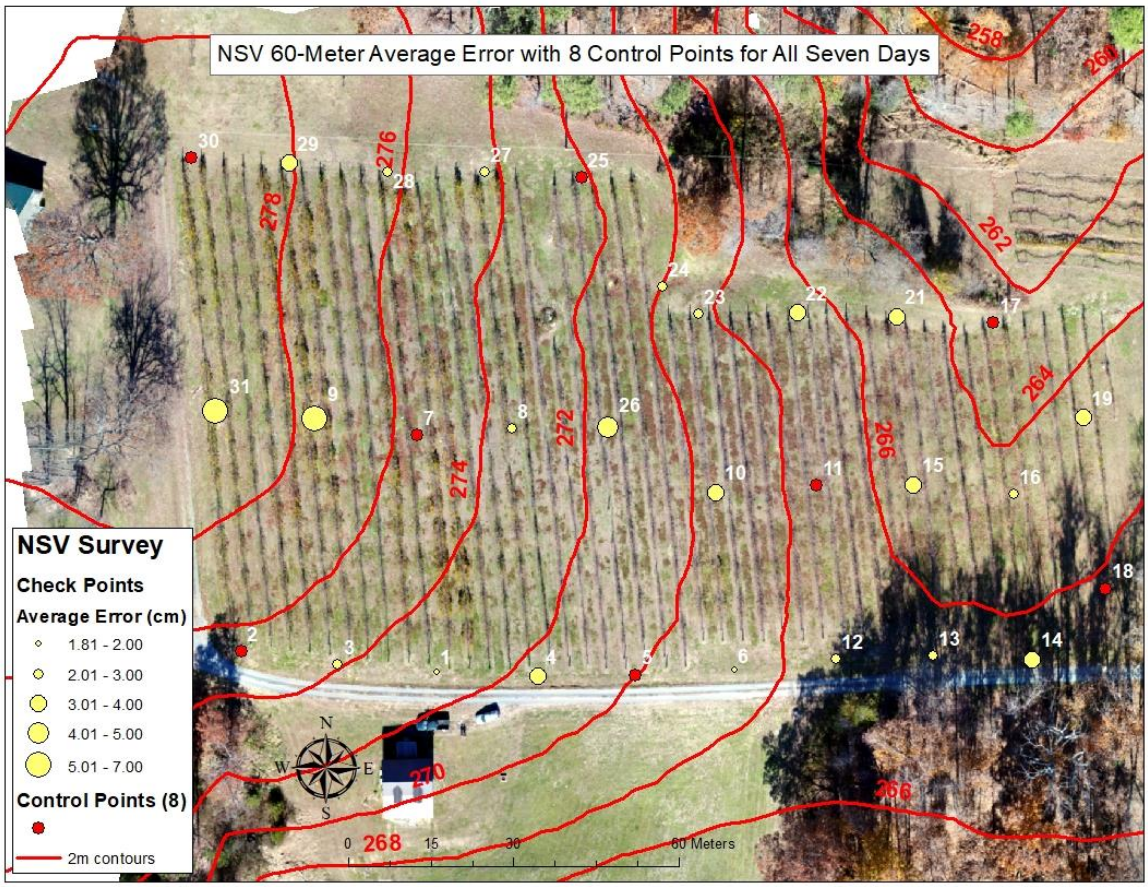

Figure 15. Average Error and Location for 60-Meter Collects Using Eight Control Points.

CHAPTER V
DISCUSSION

5.1 Altitude Comparison

This research indicates that the 80-meter data set is the most accurate for 3D modeling via SfM and thus produced the most accurate digital mapping products. The 60-meter data set was very close in accuracy outcomes and while it did not outperform the 80-meter, there was no statistically significant difference between the two. Once the flight altitude moved below sixty meters, the decreasing accuracy results started showing statistically significant differences when compared to the data from the higher altitude flights.

The altitude comparison results were interesting in that the lower altitude data sets were very similar, statistically no difference in error, and yielded lower accuracy when compared to the two higher altitude data sets. Likewise, the two higher altitude results were very similar, statistically no difference in error, and yielded higher accuracy than the lower altitude flights. Also, worth noting is that the 50-meter and 60-meter data sets were statistically different and yet they were closer in altitude than the 60-meter and 80-meter data sets. The data point to some break point between 50 and 60 meters where accuracy starts to become increasingly more affected as the UAS moves below 60 meters. Though overall

each flight became less accurate from the last with each decrease in elevation going from 4.86 cm at 80 meters to 5.68 cm at 60 meters to 7.09 cm at 50 meters and to 7.43 cm at 40 meters.

Additionally, most of the literature, and even some of the support documentation from the SfM software makers, pointed to the idea that the more images you had the better the model outcomes would be (Turner et al., 2012; Westoby et al., 2012; Torres et al., 2014; Suwardhi et al., 2015; Uysal et al., 2015). The number of images however is directly related to flight elevation and the amount of overlap used during image capture. This was held constant at 80% front and 80% side overlap for this research. This was at the high end of overlap advised in the literature and by the flight app and SfM software makers. This is probable the reason that the number of images did not play a bigger role in accuracy outcomes as the 40-meter data set had the largest image collect of all the altitudes at 156 images. The 80-meter data set had the least number of images at 52, more than a third less images than the 40-meters collect. If overlap could not be measured due to the lack of an automated flight mapping app for instance, then the rule of more images would probably be more appropriate during image collection.

While the lower altitude flights resulted in higher resolution images, they also resulted in more images taken at increasingly steeper oblique views. This would increase the distortion caused by parallax which is the displacement of the

position of an object with respect to the frame of reference as the observer moves (Wolf et al. 2014). This type of distortion increases as the observer, or camera in this case, moves closer to the object in question. If one were to hold a pencil in front of the eyes, and the head is moved side to side, the pencil would seem to move with respect to the objects behind it. The closer the object is brought to the eyes, the more significant the shift in position will appear. When performing the bundle adjustment and constructing the scene geometry, the SfM algorithm would have to average together images with a wider array of distortions (Triggs et al., 2000). This could explain why the lower altitude flights resulted in reduced accuracy and why the higher altitude flights improved the accuracy.

Finally, it is worth mentioning that collecting data at the higher altitudes also has several advantages. First, the flight times are shorter due to the fact that the image footprint is larger and thus fewer flight lines are required to cover the same area at a higher altitude compared to a lower altitude. This can make a difference in flight times and even more so as the size of the site increases. Also, by reducing flight time you also reduced the number of batteries required to complete the flight. The batteries generally only last approximately twenty minutes or so and require nearly an hour to charge.

Second, fewer images means faster processing times. Processing times were sometimes cut by as much as half when comparing processing of the 40-meter data sets with approximately 150 images to the 80-meter data sets which

averaged only 50 images. The 40-meter data sets took close to two and a half hours to process and the 80-meter data sets took just over an hour. In addition to the processing time, the manual placement of markers in the imagery is reduced significantly as the 80-meter data set contains two thirds less images. Placing the markers took one to two hours for the 40-meter data sets and less than an hour for the 80-meter. However, it is worth mentioning that the use of this 3D-modeling technique in research not involving in depth accuracy assessments would have far fewer control/check points to place markers for in processing. The actual processing time involving tie-point creation, image matching and the generation of the sparse and dense point clouds, would still be the same.

Third, flying the UAV at higher elevations reduces the risk of a collision and as mentioned earlier results in higher accuracy outcomes. Due to the mapping app's lack of ability to adjust to ground elevation changes both safety and accuracy benefit from flying at higher altitudes. At the Native Son Vineyard, the ground elevation changed from 259 meters at the lowest point to 288 meters at the highest. This is a significant amount of ground elevation variability when flying as low as forty meters. If the mapping flight began at the low end this would result in the UAS being only eleven meters from the ground when it arrives at the highest point in the vineyard. This would more than likely be below the tree canopy and could easily result in an accident and reduced accuracy outcomes from severe parallax distortion.

5.2 Ground Control and Accuracy

The results for the ground control tests were surprising in that there was very little change in accuracy across all four initial ground control scenarios. The greatest variation was found when the fifteen control points were switched with the fifteen check points. The switching of the points was used to see if the positioning of the control points, and not just the number of control points, affected the accuracy outcomes. Indeed, it did consistently affect the accuracy of the data on the first five days of flights. The first five flight days were all flown, and data collected, using the older P3P UAS.

The amount of error increased on those five flight day's data sets when the points were switched. However, the second set of points, when switched to, did not have the four control points in the corners of the site. The points were more centrally located though still evenly dispersed throughout the site. Placing control points in the corners of the area to be mapped was common in other reviewed UAS research (Turner et al., 2012; Westoby et al., 2012; Torres et al., 2014; Suwardhi et al., 2015; Uysal et al., 2015) and is also recommended for traditional aerial photogrammetry (Wolf et al., 2014). The error in the corners that no longer had control points increased while error in other areas of the orthomosaic decreased. This basically amounted to a slight reduction in accuracy and a different dispersion of the error across the site. While this is likely what caused the accuracy level to drop, none of the fifteen-control scenario switches

tested significant using unpaired t-tests. However, it seems unlikely that this would have happened by chance on every one of the P3P processed data sets.

Unexpectedly though, the last two flight days using the P4P with the improved camera showed no reduction in accuracy when the control points were switched for the check points removing the control from the corners. In fact, the accuracy from the processed data sets collected using the P4P actually improved slightly when the control and check points were switched, and corner control removed. This improvement in accuracy did not prove statistically significant however. Thus, the fluctuation could have just been the result of normal variability in the mapping process. Unlike the P3P data which had five days' worth of data to reinforce the accuracy trend, the P4P had only two days of collected data. This however, might be explained by the improved camera and shutter system producing higher quality and resolution images that are more easily interpreted by the SfM algorithms and thus are less affected by the distance between control points.

The data across all seven days showed only small variability when control was reduced. Even when the control was reduced from fifteen to eight control points very little reduction in accuracy was seen (Table 22). Only two of the five flight days using the P3P showed a significant difference at the 95% confidence interval and one day at the 90% confidence interval between the fifteen-control scenario and the eight-control scenario. The other two flight days using the P3P

showed no significance. This lends support to their only being a need for limited control on the ground to achieve sub decimeter accuracy even when using a low-cost camera and UAS. It was unexpected that almost no change in accuracy would be seen as the control was reduced to as low as eight points. In the original research design this was the lowest level of control and it was expected to yield a higher difference in the accuracy outcomes. For this reason, the research design was altered to take the most accurate of the flight days down four more levels of reduced control.

Four additional control scenarios were added to the day six data set. The flight data from this day were chosen because it yielded the highest accuracy levels. It was also one of the flight days using the P4P with the improved camera. Control was reduced first to six points and the error increased from 2.519 to 2.736 cm. As the control was reduced to five, the error increased again dropping from 2.736 to 3.015 cm. It wasn't until dropping the control to four points, with the error going from 3.015 to 3.837 cm, that the error change started testing significant at 90% confidence interval using the paired t-tests. The final reduction in control, reducing to three control points, resulted in the error dropping to 7.513 cm and reaching a 95% confidence interval (Table 20).

This finding was significant as it clearly identifies the level of control where accuracy starts to become significantly affected. Even using only five control points there is very little loss of accuracy. Reducing control from fifteen to five

only reduced the total RMS error by .293 cm. In fact, the reduction in accuracy was so low that it was not statistically significant. The four-control scenario, testing significant at the 90% confidence interval, should not be overlooked as it increased the total RMS error by 1.114 cm to total of 3.837 cm. This is a comparable error rate seen from several of the other flights using the P3P UAS. However, the biggest issue becomes the maximum single point errors which reached as high as 9.875 cm under the 4-control scenario. The maximum single point error under the 3-control scenario was as high as 15.196 cm.

Also, worth noting is that as the control was reduced each time, the removed points were added to the error check making it even more robust. The final five-control scenario was error checked using 25 points throughout the vineyard. Of the three coordinate parameters, x, y, and z, the highest error found across all the twenty-five check points was only 4.518 cm in the z-coordinate. The highest total error for any check point under the five-control scenario was only 5.231 cm. While the total RMS error for each data set is important, these maximum value errors are also important as they indicate areas where the SfM algorithm is having difficulties recreating the scene geometry. The difficulties are most likely an indication of the lack of control in that location. The largest error found across the entire site was only 5.231 cm supporting the notion that the quality of the models produced from a low-cost UAS/camera were high and comparable to other higher cost solutions. The applications for this

modeling/mapping approach should be broad and acceptable under even some of the strictest geomatics requirements.

Finally, there seemed to be some correlation between accuracy and the varying topography at the site. The elevation increased from east to west by as much as twelve meters within the survey area of the site. The west end of the vineyard did show higher error rates in a few locations, but this was attributed to the reduced number of images overlapping in that area. However, as was previously discussed in the altitude section, the reduced overlap was caused by the UAS not compensating for the ground elevation change. Though this has yet to be tested, adding a buffer area of ten to twenty percent around the site might compensate for the overlap loss due to ground elevation change at the edges. Starting the flight at the highest elevation point within the site could also be another method to stop the UAS from moving closer to the ground during the flight.

Additionally, elevation data could be incorporated into the flight planning software, but it would need to be to be of a resolution high enough to model the relief of a site this small. The MapPilot flight planning software offers elevation data that can be used by the app for altering the elevation during flight, but the resolution of the data is so coarse that it would have no effect at a study site as small as the vineyard. Currently, the app does not allow for the uploading of user data to be used in lieu of the elevation data supplied by the app maker. The

elevation issues, however, were not dramatic and the SfM algorithm implemented in the PhotoScan software proved to be robust in rendering the scene geometry under the topographic conditions found at the study site. This is proven evident by the accuracy results obtained during the course this research.

5.3 Image Overlap, Camera Locations and X, Y and Z Error

The western end of the vineyard had lower image overlap numbers when compared to any other location within the survey area. This means that there were fewer overlapping images involved in the recreation of the scene geometry used to create the dense point cloud and orthomosaic. Figure 16 shows an image overlap map with camera locations from day six at the 60-meter and eight control point scenario. The black dots are the locations of the camera when each image was taken during flight. The darkest blue areas in the map are the areas of optimum overlap and where more than nine images were used in scene recreation.

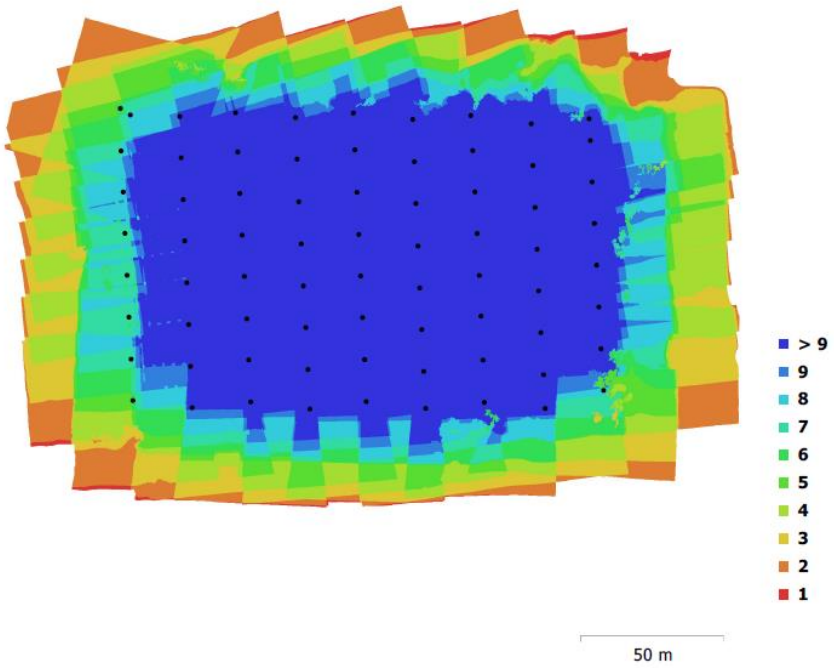

Figure 16. Camera Location and Image Overlap from Day Six at 60-Meters.

When the UAS flies a preprogrammed flight path it doesn't compensate for elevation changes. This is not currently available for a site this small within the current iteration of the MapPilot app. For this reason, when the UAS flies over areas of increasing elevation the image foot print decreases in size. In the case of the site used in this research, there was a change in elevation of twelve meters going from the east end of the vineyard to the west end. This caused the UAV to fly an image overlap pattern for a sixty-meter flight altitude at forty-eight meters at the west end of the site.

The MapPilot algorithm built a flight pattern for the image foot print at sixty meters. As the ground elevation increased to the west, the camera began

capturing increasingly smaller areas. By the end of the flight, the image foot print would have decreased to the point that it was no longer capturing an eighty percent front and side overlap. This would have a more significant effect at the edges of the study area than regions more towards the interior. As a result, regions of the interior would still have overlap on all four sides while edges would only have overlap in the front, back and interior facing side. Thus, there are no images to compensate for the loss of overlap at the exterior edge of the site.

Figure 17 shows the orthomosaic generated from PhotoScan with x, y and z errors associated with each check and control point. The x and y errors are depicted using the shape and size of an ellipse, while the z errors are depicted using colors in a way similar to a choropleth map. The ellipses are exaggerated by the value located in the bottom right of the map, which in this case is 200 times. This allows the shape and trajectory to be more easily be seen. Figure 17 is also from the day six flight at the 60-meter and eight control point scenario. This was the most accurate of all the flights under that scenario. When moving from right to left across the map it can be noticed that the ellipses become more and more elongated. This is especially true as one moves into the north west corner of the map where the elongation of the ellipses is most severe, and the elevation change is at its peak.

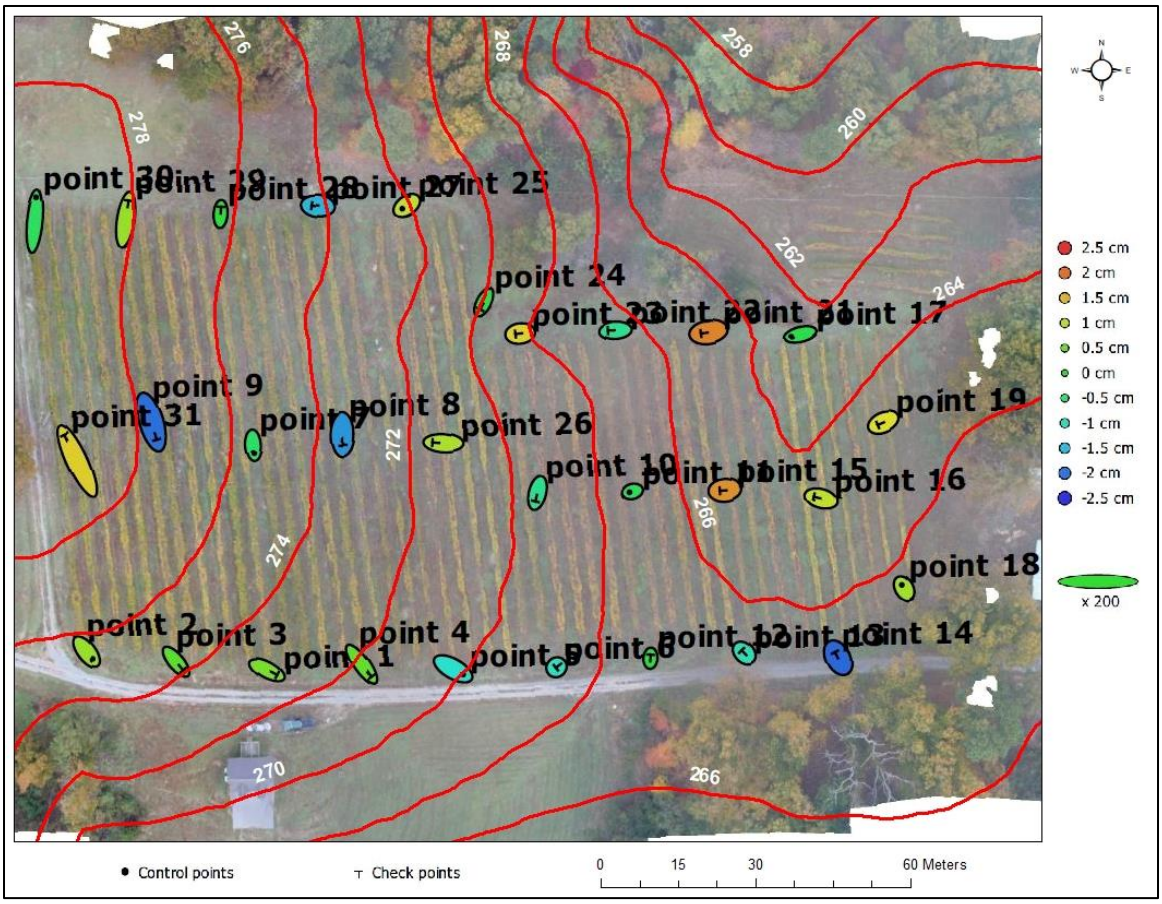

Figure 17. X, Y and Z Error from Day Six at 60-Meters and Eight Control Points.

The image overlap and camera location maps (Figure 16) indicate that when mapping a site, it would be advisable to increase the area of image collection beyond the desired area of interest. It is important that all terrain to be modeled fall within the dark blue areas of the image overlap maps. When there are elevation changes within a study site of more than ten meters it is even more important to increase the collection area due to the variability in the image foot print discussed earlier.

Check Point thirty-one (Figure 17) was the point with the highest error and was in the area that fell outside the optimum overlap zone. Check point nine was the point with the second highest error and was the closest check point to check point thirty-one. Check point nine did fall within the dark blue optimum overlap zone, however, it is possible that it is being distorted by the model's subpar scene geometry construction around the area of point thirty-one due to the lack of overlap in that area. A similar situation was seen when a target was misplaced in the field and caused the surrounding survey points to be dragged in the direction of misplacement when processed in the lab.

The increase in the collection area does not have to be significant as most of the vineyard fell within the dark blue areas of the image overlap map. In this study, a ten to twenty percent increase in the area would be more than enough to ensure the desired area to be modeled is well within the optimum overlap zone. If the surrounding area is available for use as part of the flight path, then there is no reason to not incorporate it into to the model as a buffer. The buffer areas, if unwanted, can always be clipped out after processing.

One issue that arose from increasing the flight area is that there is an increase in the chance of having obstructions interfere with the flight path. The biggest problem arises from large trees and variable terrain elevation in and around the location to be mapped. This was indeed the case at the Native Son Vineyard where large trees surrounded the vineyard on three of the four sides.

The trees on the west end of the vineyard were within ten meters of the last row of vines. The elevation also increased from east to west making the west end of the vineyard as much as twelve meters higher near the location of the trees.

Low altitude flights require careful attention to the flight path and elevation changes. The 40-meter flights at the research site would have flown right into the trees, which were approximately thirty meters in height, as the UAS flight path moved from the east end to the west end. This was due to the topography of the site and that the UAS does not compensate for the ground elevation change. This also presents a good example of how the higher altitude flights are safer for collecting data when using an automated flight control app like the one used in this research.

5.4 Rolling Shutters and Global Shutters

For this study the P3P and P4P cameras were compared. The P4P UAS had a 20-megapixel camera with a global shutter and the P3P had a 12.4-megapixel camera and a rolling shutter. Additionally, the 'fit-to-rolling shutter' option within PhotoScan was included in the comparison. Table 24 shows the flights and associated errors for each camera type and processing parameters. The 20-megapixel camera on the P4P UAS produced the best overall accuracy with a total RMS error of 2.519 cm on day 6 at the 60-meter altitude using the eight-control point scenario. The P3P was less accurate without correction, producing a total RMS error of 8.206 cm. However, the P3P data processed,

using the ‘fit-to-rolling shutter’ option, was far more accurate with a total RMS error of 3.744 cm.

Table 24. Accuracy Data from Day Five and Day Six Showing Rolling Shutters from the P3P with and Without Correction and the Global Shutter from the P4P Without Correction.

Flight	Check	X Err (cm)	Y Err (cm)	Z Err (cm)	XY Err (cm)	Tot (cm)	Fit to Rolling	Shutter Type
NSV_60m_D5_5	22	4.197	6.510	2.710	7.746	8.206	No	Rolling
NSV_60m_D5_5	22	2.578	1.582	2.205	3.025	3.744	Yes	Rolling
NSV_60m_D6_5	22	1.206	1.853	1.206	2.211	2.519	No	Global

Table 25 shows the three paired two sample for means t-tests for the rolling and global shutter comparison using a 95% confidence interval. The null hypothesis states that there is no significant difference in the data sets. The first t-test (Table 25) compares using the ‘fit-to-rolling shutter’ option to the same data processed without using the option (uncorrected). A p-value of 0.00002 was obtained for the comparison and thus the null hypothesis was rejected. The second comparison (Table 25) was between the uncorrected shutter and the global shutter from the P4P UAS. A p-value of 0.00000002 was obtained and also resulted in rejected the null hypothesis. Finally, the third comparison (Table 25) between the corrected data set, using ‘fit-to-rolling shutter’ option, from the P3P and the global shutter data set from the P4P resulted in a p-value of 0.0015 also rejecting the null hypothesis.

$H_0 : \mu_d = 0$
$H_1 : \mu_d \neq 0$ (two-tailed)

Table 25. Paired Two Sample for Means T-Tests for the Rolling and Global Shutter Comparison.

Flight Path Type		P(T<=t) two-tail	t stat	t Critical two-tail
NoFitRoll_Total(cm)	FitRollTotal(cm)	0.00002668	5.34472	2.07961
NoFitRoll_Total(cm)	GlobTotal(cm)	0.00000002	8.76598	2.07961
FitRollTotal(cm)	GlobTotal(cm)	0.001513971	3.64480	2.07961

While the accuracy for P3P was greatly improved using the 'fit-to-rolling shutter' option, the image resolution is unchanged. The P4P camera produced a better clarity on the ground when compard to the P3P imagery. This can be seen in Figure 18 which shows the 60-meter orthomosaic zoomed into survey point 14. The image on the left is taken from the P4P orthomosaic and image on the right is from the P3P orthomosaic. The ground resolution for the P4P was 1.6 cm/pix compared to 2.37 cm/pix ground resolution for the P3P using the same flight parameters at 60-meter altitude. These ground resolution values were determined by the PhotoScan Professional image processing software. The 32.5% increase in resolution was attributed to the 40% increase in megapixels of the P4P camera.

Figure 18. 60-Meter Orthomosaic Images Showing the Difference in Clarity Between the P4P (Left) and P3P (Right) Cameras, Respectively.

The difference in the shutter types cannot be overstated. The improved technology of the global shutter significantly outperformed the rolling shutter in the level of accuracy produced in the digital mapping products generated from PhotoScan Professional. The majority of the error in the rolling shutter was found in the x and y coordinates and small differences in the z coordinate. The slower exposure causes blurring across the image when the UAS is in motion. The effect would drag the image out in the direction of flight and have a stronger distorting effect in the x and y coordinates. In other words, objects in the scene would appear slightly elongated. The error amounts for the rolling shutter equipped UAS were nearly three times the error amounts seen with the global shutter equipped UAS.

PhotoScan's option to correct for the rolling shutter was shown to work exceptionally well. The 'fit-to-rolling shutter' option reduced the total RMS error of the rolling shutter data set from 8.206 cm to 3.744 cm. Even with the correction,

however, the rolling shutter data set underperformed when compared to the global shutter with a total RMS error of 2.519 cm. This is more than a centimeter better in total accuracy. This may not sound significant until one considers that the total RMS error for the global shutter data set was only 2.519 cm, or nearly fifty percent of the total error.

Another important factor between the two cameras was the difference in mega pixels. The older rolling shutter equipped camera was rated at 12-megapixels while the newer model camera with the global shutter was 20-megapixels. There is no way to be certain from this research that the improved resolution in the camera with the global shutter did not have any impact on the accuracy outcomes. This was not tested; however, the data indicates that the additional clarity in the imagery would have some impact on the accuracy.

This was visually obvious during the marker placement procedure in PhotoScan. It was easier to find and place the digital markers in the center of the targets with the imagery taken from the improved camera model fitted with the global shutter and increased megapixels. Accuracy is directly affected by how well the user is able to place these markers representing the spot in the imagery where the survey points are located. This is, however, objective and would require additional testing and was not performed in this research.

5.5 Flight Paths

Three different flight paths were used in this dissertation across the seven days of data collects (Table 26). The comparison between flight paths were completed by using the P3P at 60-meters and under the eight-control point scenario. The widthwise flight path was considered the standard flight path and was used on all flights other than the two lengthwise flight paths and the single diagonal flight path (Figure 19). The highest error of 5.147 cm was produced using the diagonal flight path. The lowest error was produced using the lengthwise flight path at 3.223 cm. However, the lengthwise and widthwise were very close in accuracy with the lengthwise flight path producing error both above and below the widthwise results. Figure 19 shows the actual flight paths taken from the Map Pilot app. The widthwise flight path is on the left with lengthwise in the middle, and the diagonal on the right (Figure 19). All flight paths flown using the P4P were completed using the widthwise flight path and thus were not included in the flight path comparison.

Table 26. Comparison of Three Different Flight Paths from Days Three, Four, and Five.

Flight	Check	X Err (cm)	Y Err (cm)	Z Err (cm)	XY Err (cm)	Tot (cm)	Flight Path
NSV_60m_D3_5	22	1.817	2.443	3.264	3.045	4.464	Lengthwise
NSV_60m2_D4_5	22	1.477	1.309	2.548	1.974	3.223	Lengthwise
NSV_60m_D4_5	22	2.875	1.671	2.691	3.326	4.279	Widthwise
NSV_60m2_D5_5	22	2.164	1.594	4.390	2.687	5.147	Diagonal
NSV_60m_D5_5	22	2.578	1.582	2.205	3.025	3.744	Widthwise

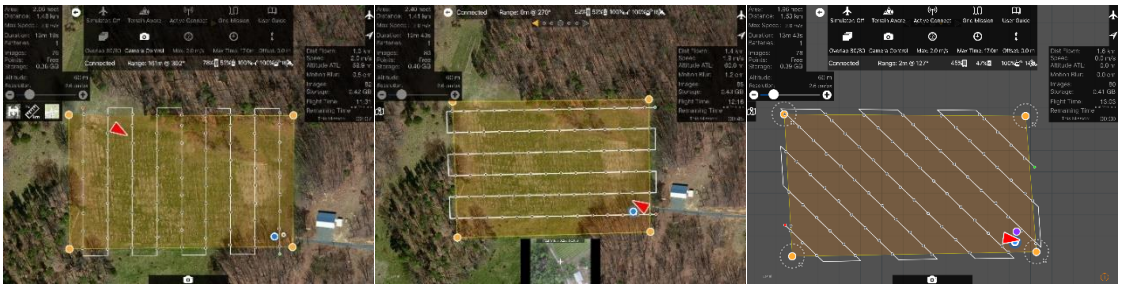

Figure 19. Three Different Flight Path Types Shown from Left to Right in the MapPilot App: Widthwise (Left), Lengthwise (Middle), and Diagonal (Right).

Table 27 shows the paired two sample for means t-tests for the five flights used in the comparison. The null hypothesis stated that there was no significant difference in the data sets. The comparison between the lengthwise flight from day five and the diagonal flight from day four resulted in a p-value of 0.0021 rejecting the null hypothesis. The day four lengthwise flight data set rejected the null hypothesis when compared to both the widthwise from day four and the other lengthwise from day three. Additionally, the diagonal from day five rejected the null hypothesis when compared to the widthwise flight data set from day five.

$H_0 : \mu_d = 0$

$H_1 : \mu_d \neq 0$ (two-tailed)

Table 27. Paired Two Sample for Means T-Tests for the Flight Path Comparisons.

Flight Path Type		P(T<=t) two-tail	t stat	t Critical two-tail
Lengthwise *60m2_D4_5_Total(cm)*	Lengthwise *60m_D3_5_Total(cm)*	**0.01201002**	2.74958	2.07961
Lengthwise *60m2_D4_5_Total(cm)*	Widthwise *60m_D4_5_Total(cm)*	**0.010636637**	2.80388	2.07961
Lengthwise *60m2_D5_5_Total(cm)*	Diagonal *60m2_D4_5_Total(cm)*	**0.00214632**	3.49723	2.07961
Diagonal *60m2_D5_5_Total(cm)*	Widthwise *60m_D5_5_Total(cm)*	**0.017469191**	2.57984	2.07961

The results of the flight path tests were inconclusive regarding the lengthwise and widthwise flight paths. Both performed well and yielded similar results regarding error outcomes. The assumption was that since the rows of vines ran widthwise, they might obscure the camera's view under and around the vines. This did not seem to be the case as PhotoScan was able to recreate the scene geometry under and around the vines in all flight scenarios. The resulting errors for points within the vineyard were not statistically different form the point errors located along the edges where the vine rows did not obscure the targets.

The diagonal, or angled, flight path resulted in the highest error outcome of all three flight path types. The total RMS error for the data set from that flight was the highest of any of the flights flown across all seven days at the vineyard. However, only one flight was flown using this method and more flights would be

needed to draw conclusions about its effectiveness in UAS mapping. The results might have been more variable had larger number of flights been flown using the diagonal flight path. The diagonal flight path did test significantly different from the other two flight paths though and an early recommendation would be to use one of the other flight paths, lengthwise or widthwise, for future work until further testing can be done.

5.6 Target Types

Two different two-foot by two-foot target types, the triangle and checker pattern (Figure 20), were used to investigate whether ground targets could influence accuracy outcomes. The triangle was used as the standard target as the other target type was not created until half way through the field work. Table 28 shows the error outcomes for the two types of targets flown at the 60-meter altitude using the eight-control point scenario. The checker pattern yielded slightly higher accuracy with a total RMS error of 3.784 cm while the triangle pattern was 4.279. These two flights were flown on the same day under the same parameters other than the targets.

Table 28. Accuracy Assessments for Two Flights on Day Four Using Alternate Target Types.

Flight	Check	X Err (cm)	Y Err (cm)	Z Err (cm)	XY Err (cm)	Tot (cm)	Target Type
NSV_60m_D4_5	22	2.875	1.671	2.691	3.326	4.279	Triangle
NSV_60m3_D4_5	22	2.377	1.755	2.364	2.954	3.784	Checker

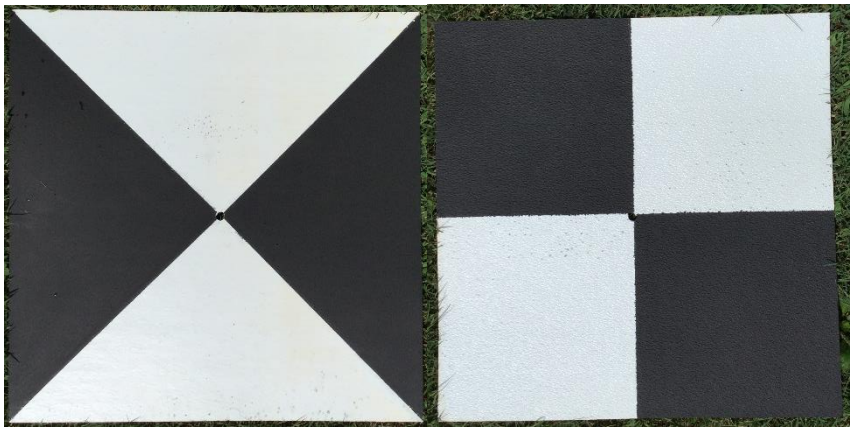

Figure 20. The Triangle and Checker Targets, Repectively.

A paired two sample for means t-test was used in the comparison between the two target types based on the total RMS error. The null hypothesis states that there is no significant difference in the data sets. The t-test resulted in a p-value of 0.0143 and thus rejected the null hypothesis at the 95% confidence interval.

$$H_0 : \mu_d = 0$$

$$H_1 : \mu_d \neq 0 \text{ (two-tailed)}$$

The target types tested significantly different at the 95% confidence interval. This was a bit surprising in that the two target types were very similar.

Both flights in the test used the same P3P UAS with the older camera type. The imagery from the older P3P UAS yielded lower image quality and resolution causing the marker placement in PhotoScan to be visually difficult at times. Any improvement in finding the center point of the aerial target in the images directly results in improved accuracy.

Under high light conditions the targets suffered from oversaturation (Figure 21) causing the white areas of the target to overwrite the black areas. This would result in greater difficulty finding the center point and it required a high degree of concentration and in some cases subjective placement. The checkered target pattern seemed to suffer less from oversaturation which would have caused marker placement in PhotoScan to be visually easier and thus affecting the final total RMS error results. However, light levels were not monitored in a way that would allow for accurate testing. During the research design it was not anticipated that the light levels would have such a strong effect on the appearance of the targets in the imagery.

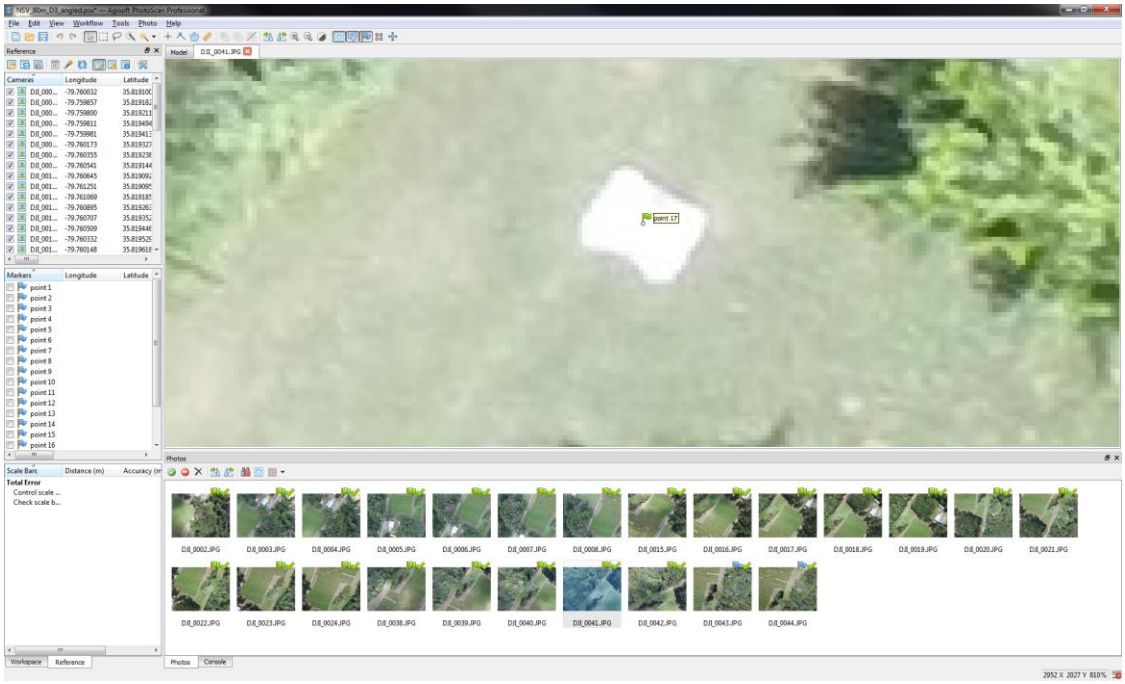

Figure 21. Oversaturation of the Aerial Targets Under High Light Conditions.

The P4P was not used in the target comparison, however, the imagery from the P4P was superior in clarity compared to the imagery from the P3P. This made marker placement easier as the aerial targets were clearer and less distorted. The imagery from the P4P also seemed to suffer less from oversaturation. However, the biggest factor influencing oversaturation was the amount of light. Sunny conditions generally led to reduced target clarity while overcast conditions appeared to result in the best view of the targets.

5.7 Processing with Targets Left in the Field Compared to Manual Removal

In georeferencing the point clouds at different levels of control, the aerial targets were simply switched from control points to check points within PhotoScan. These targets were physically left in the study area and visible to the processing algorithms. To test whether the targets left in the field might influence accuracy, additional flight tests were performed manually removing the targets from the study area in the same order they were removed using the PhotoScan software. It was thought that by leaving easily discernable features on the ground it might be providing the PhotoScan algorithm additional tie points. Those additional tie points would not have been there under normal circumstances and thus could influence accuracy outcomes.

Table 29 shows the accuracy outcomes for two flights using the P4P UAS under the same flight parameters at the 60-meter altitude. The manual removal of the targets resulted in a slightly more accurate outcome with a total RSM error of 1.934 cm. The comparisons of the two data sets however did not prove significant at the five or ten percent significance using the paired or unpaired t-tests.

Table 29. Accuracy Comparison of Two 60m Flights on the Same Day with Targets Removed Manually in the Field and the Other Processed with All Targets on the Ground.

Flight	Control	X Err (cm)	Y Err (cm)	Z Err (cm)	XY Err (cm)	Tot (cm)	Target Removal
NSV_60m_D7_2	14	0.735	1.490	0.989	1.662	1.934	Manual
NSV_60m_D7_2	15	0.786	1.549	1.095	1.737	2.053	PhotoScan

Paired two sample for means t-tests for the two flights used in the target removal comparison can be seen in Table 30. The null hypothesis states that there is no significant difference in the data sets. The p-value for the t-test comparing total error was 0.154. Therefore, the null hypothesis could not be rejected at the 95% confidence interval. Since this compares only total linear distance error and not error in a three-dimensional coordinate system, t-test were performed on each of the three coordinate parameters separately to verify that there were no differences between the x, y or z coordinates. All three of these coordinate values, x, y and z, failed to reject the null hypothesis supporting the notion that any differences in error between these two target removal methods were simply due to random variability in the UAS mapping process.

$$H_0 : \mu_d = 0$$

$$H_1 : \mu_d \neq 0 \text{ (two-tailed)}$$

Table 30. Paired Two Sample for Means T-Tests for the Two Flights Used in the Target Removal Comparison.

t-Test: Paired Two Sample for Means		P(T<=t) two-tail	t Stat	t Critical two-tail
60m_D7_2_Total (cm)	*60m_D7_2Man_Total(cm)*	0.154469285	1.52911	2.2009
Xerror (cm)	*Man_Xerror (cm)*	0.428749321	0.82160	2.2009
Yerror (cm)	*Man_Yerror (cm)*	0.578925478	0.57184	2.2009
Zerror (cm)	*Man_Zerror (cm)*	0.801993689	0.25690	2.2009

The removal of targets manually versus the process done digitally in PhotoScan was shown to have no effect on accuracy. In fact, the accuracy was higher in the data set where the targets were removed manually from the field. Since none of the t-tests proved significant it is assumed that simple variation in the mapping process led to the differences seen between the two data sets. This is not surprising in that there is a great deal of subjective work done in PhotoScan to tie each aerial target to its survey point location. The software attempts to do this automatically, but a human adjustment is almost always required to achieve higher accuracy. The user's eyesight, dexterity and attention to detail play a large role in the process.

5.8 Suitability for Monitoring Change

This section is not intended to be a comprehensive quantitative analysis of using data from a low cost UAS in change detection. It is simply intended to provide a brief synopsis of what was found during this dissertation research, which focused primarily on other factors regarding using data from a low cost UAS for mapping and modeling terrain. However, the factors explored in this research are important building blocks for UAS applications in monitoring change

on the surface of the Earth. Understanding how UAS data collection is affected by altitude, flight patterns, ground control, lighting and aerial targets provides critical information needed for change detection research involving a UAS. The reason is that these factors, as documented in this research, influence the accuracy and quality of the digital modeling and mapping products and are critical to understand before perusing change detection research that implements a UAS.

One of the more important findings from this research for change detection involves the temporal aspects and repeatability/registration of the UAS data collection (Jensen 2016, p.504). Temporally speaking, data collection using a UAS is extremely flexible and is unsurpassed by any other method. Manned flight is costly, requires a great deal of planning and cannot easily be delayed an hour or a day due to weather. With satellite imagery, researchers are generally left with whatever they can get from pre-capture imagery archives and have no control over when the data is collected. However, using UAS, the researcher has nearly full control over when and how the data are collected. If conditions are not perfect, you simply wait until they improve. This allows a much greater ability to match the conditions present during the last data collect resulting in improved change detection outcomes.

Image registration/repeatability is an important factor when using multiple images in change detection (Radke et al. 2005; Jensen 2005; Jones et al. 2017).

The small variance between model accuracy found in this research should allow for image registration suitable for monitoring change at a very high resolution. The average standard deviation in accuracy between the check points in the models flown at sixty meters and using eight-control points was 1.121 cm. The largest standard deviation for any check point in the models flown at sixty meters and using eight-control points was 2.026 cm.

Figure 22 shows orthomosaics from day five and day six in ArcGIS Pro using the swipe function to illustrate vegetative change on the ground over time. A rock protruding out of the ground and outlined by a red box can be seen aligning nearly perfectly between both dates of orthomosaics (Figure 22). Figure 23 shows the orthomosaics from day five and day seven displaying the same location as seen in Figure 22 and using the same swipe method. Figure 24 shows survey point ten from the survey shapefile overlaid onto the orthomosaics from day seven on the left and day five on the right. The survey shapefile points coincide almost perfectly with where the center point of the target is in both data sets from two different UASs and on two different days. It is worth noting that the P4P was used in the day seven data collect and the older P3P was used to collect the data for the day five data. The clarity difference is clearly visible in the two images (Figure 24).

Figure 22. Day Five (9/10/17) to Day Six (11/5/17) Registered Images Swiped in ArcGIS Pro.

Figure 23. Day Five (9/10/17) to Day Seven (11/5/17) Registered Images Swiped in ArcGIS Pro.

Figure 24. Survey Point Ten Seen in the Orthomosaic on Day Seven from P4P and Day Five from P3P, Respectively.

Methods tested, and evidence presented in this research shows that UASs should prove to be more than capable of supporting change detection research agendas. However, the mapping products produced from UASs are different from imagery typically used in change detection in that they are point clouds which are textured and colored to represent the scene as if it was one image. However, it is not one image, and in some instances, you can find flaws in the scene being modeled. Figure 25 shows powerlines that do not line up correctly and illustrate some of the challenges that researchers need to be aware of when using this imagery for change detection and other types of research.

Figure 25. Structure from Motion Flaws Seen in the Misaligned Powerlines.

CHAPTER VI
CONCLUSION AND FUTURE RESEARCH

The use of a low-cost UAS in collecting imagery for use in modeling and mapping applications has been found to be reliable and reproducible, and yields a sub decimeter level of accuracy. It truly represents a new level of scale available to researchers that was previously unattainable and at a low cost. The products produced from this process allow researchers the ability to more easily move to larger scale data sets, helping answer questions in a variety of research agendas that cannot be answered with smaller scale data sets.

This research has revealed information regarding altitude and ground control that will prove vital for future research involving the use of UASs in mapping and modeling of the environment. Optimum data collection altitude was not revealed in any of the literature reviewed for this dissertation making this a novel discovery. The idea that a lower altitude would reduce accuracy was completely counter intuitive to the thought process going into this research. This finding provides reassurance to future researchers that flying at safer altitudes of sixty plus meters will not sacrifice accuracy levels and may actually improve them. The eighty-meter flight altitude is safer and saves time both during collection and processing adding even more benefit to the finding.

Additionally, the ground control findings identify the exact point where accuracy begins to falter revealing the optimum number of ground control points needed (five) for the highest levels of accuracy obtainable with a low cost UAS at a site of this type. One ground control point per acre proved to be the optimum number of control regarding accuracy for this site. Reducing ground control to as low as three points also reveal how even a small number of ground control points can generate mapping products with a total RMS error that was still sub decimeter. This is incredibly useful information for researchers that do not need the highest degree of accuracy. Meanwhile, researchers looking to obtain highly accurate survey grade results will find that as few as five ground control points can produce mapping products with a total RMS error hovering between 2 to 3 cm. Moreover, those results were shown to be repeatable.

Topography was shown in this research to impact accuracy due to the influence it has on the image foot print size. This, in turn, would cause the programmed overlap to vary during flight resulting in areas around the perimeter of the site that would fall below the optimum overlap range for scene reconstruction by the SfM software. Identifying this will aid future research by helping to recognize areas of a site that might cause this problem, resulting in the need to recapture data. Terrain that varies toward the edges of the site by more than ten meters will be most susceptible to this problem.

The global shutter system and higher megapixel camera of the P4P resulted in much better image quality and was also shown to improve accuracy. The clarity generated by the improved camera allowed for easier and more accurate image processing due to the reduced visual strain during marker placement. All cameras are not alike and picking a UAS that has a global shutter and higher megapixel rating does make a significant difference in the final mapping products. This will be a significant factor for someone selecting a UAS for research.

Aerial targets are an integral part of conducting research that will be implementing a UAS. It has been shown here that targets do have an influence on the final mapping products and accuracy outcomes. The pattern and coloring play a role in how the target will appear in the imagery that will be used by the SfM software. This factor, in conjunction with image clarity, impacts the user's ability to identify and place referencing markers during processing. Additionally, lighting strongly influences the appearance of the target and was shown to cause oversaturation to the point that the target would appear as a single white square. Future researchers will want to pay close attention to the lighting and target style used during data collection.

None of the three flight paths tested during this research stood out as significantly better than the others. However, this in itself will be beneficial by signaling to future researchers that there might be better areas to focus on to

improve data collection. It is important to note, though, that different sites may provide scenarios that could be impacted more by the flight path choice. So, while this research shows that it should not be at the top of the list of concerns for data capture, it should definitely still be kept under consideration.

There is a multitude of future research avenues stemming from this dissertation. The aerial targets have the ability to influence accuracy and this research only scratched the surface of the possible target types, sizes and coloring that might affect the accuracy and ease of processing. A bullseye type target was suggested by PhotoScan support technicians. Also, investigating colors that have a reduced chance of becoming oversaturated in high sun light would also be beneficial in future research.

Further work regarding ground control and placement of the survey points under different terrain conditions is needed to more thoroughly understand the impact of topography on accuracy. While the vineyard provided a unique and challenging set of conditions to model, there are an endless number of other conditions in which to investigate. Additionally, the modeling of structures/features to incorporate within a terrain model would be beneficial especially in archaeology and cultural preservation research.

Monitoring change on the surface of the Earth through the use of UASs is going to reveal a great deal of information regarding Earth system processes. The temporal aspects and high spatial resolution of UAS imagery will open

research avenues that were simply to costly or to difficult to pursue. For instance, geomorphology and environmental research agendas investigating erosion, stream channels, and vegetation under influences of change will find these data collection tool of great importance. Collecting data at specific times, such as right before and right after a storm, will be instrumental in understanding the changing landscape and how these natural processes affect them.

One hurdle for UAS use is getting licensed at both the state and federal levels. The federal license must also be renewed every two years and requires the UAS pilot to stay current with all laws and regulations. Permission to fly the UAS legally in your area of interest is also still very challenging. However, by following the rules laid out by the FAA and building trust with the landowner's, future use of UASs in research is very promising.

REFERENCES

Arya, S., Mount, D.M., Netanyahu, N.S., Silverman, R. and Wu, A.Y., (1998). “An optimal algorithm for approximate nearest neighbor searching fixed dimensions”. *Journal of the Association for Computing Machinery.* 45: 891-923.

Avery, T.E. and Graydon, L.B. (1992) Fundamentals of Remote Sensing and Airphoto Interpretation. New York; Toronto; New York: Macmillan ; Maxwell Macmillan Canada ; Maxwell Macmillan International.

Bendig, J., Willkomm, M., Tilly, N., Gnyp M.L., Bennertz, S., Qiang, C., Miao, Y., Lenz-Wiedemann, V.I.S. and Bareth, G. (2013). “Very High Resolution Crop Surface Models (CSMs) from UAV-Based Stereo Images for Rice Growth Monitoring In Northeast China.” *ISPRS - International Archives of the Photogrammetry, Remote Sensing and Spatial Information Sciences.* August: 45–50.

Clapuyt, Francois, Veerle Vanacker, and Kristof Van Oost (2016). “Reproducibility of UAV-Based Earth Topography Reconstructions Based on Structure-from-Motion Algorithms.” *Geomorphology, Geospatial Sciences - Acquisition and Processing for 21st Century Geomorphological Challenges*. 260: 4–15.

Chai, T., and R. R. Draxler. 2014. "Root mean square error (RMSE) or mean absolute error (MAE)?" *Geoscientific Model Development Discussions*. 7 (1): 1525-1534.

Colomina, I., and P. Molina (2014). “Unmanned Aerial Systems for Photogrammetry and Remote Sensing: A Review.” *ISPRS Journal of Photogrammetry and Remote Sensing.* 92: 79–97.

Everaerts, J., D. Fransaer and Lewyckyi N. (2018). “Pegasus: Design of A Stratospheric Long Endurance UAV System for Remote Sensing.” *International Archives of Photogrammetry Remote Sensing and Spatial Information Sciences*. 35: 29–33.

Fausta Fiorillo, Belén Jiménez Fernández-Palacios (2015). “3d Surveying and Modelling of the Archaeological Area of Paestum, Italy”. *Virtual Archaeology Review*. 8:55.

Fernández-Hernandez, J., D. González-Aguilera, P. Rodríguez-Gonzálvez, and J. Mancera-Taboada (2015). “Image-Based Modelling from Unmanned Aerial Vehicle (UAV) Photogrammetry: An Effective, Low-Cost Tool for Archaeological Applications.” *Archaeometry*. 57: 128–45.

Fausta Fiorillo, Belén Jiménez Fernández-Palacios (2015). “3d Surveying and Modelling of the Archaeological Area of Paestum, Italy.” *Virtual Archaeology Review*. 4, 8: 55.

Fischler, M.A., Bolles, R.C., (1987). Random Sample Consensus: a paradigm for model fitting with applications to image analysis and automated cartography. In: Martin, A.F., Oscar, F. (Eds.), Readings in Computer Vision: Issues, Problems, Principles, and Paradigms. Morgan Kaufmann Publishers Inc., London, pp. 726-740.

Fransaer, D, N Lewyckyj, F Vanderhaegehen, and J Everaerts (2004). “Pegasus: Business Model for A Stratospheric Long Endurance UAV System For Remote Sensing.” International Archives of Photogrammetry Remote Sensing and Spatial Information Sciences. 35: 625–29.

Furukawa, Y., Ponce, J., (2007). Accurate, dense, and robust multi-view stereopsis. *Proceedings, IEEE Conference on Computer Vision and Pattern Recognition (CVPR)*. 17-22 June, Minneapolis, USA, pp. 1-8.

Goodchild, M.F., (2001). Models of scale and scales of modeling, in N.J. Tate and P.M. Atkinson (eds). *Modelling Scale in Geographical Information Science.* (Chichester: John Wiley and Sons) 3–10.

Jensen, John R. (2005). Introductory Digital Image Processing: A Remote Sensing Perspective. Upper Saddle River, N.J.: Prentice Hall.

Jones, M. K., DeBell, L., Quine, T. A., Lark, M., Rickson, J. and Brazier, R. E. (2017). "Testing the Utility of Structure-from-Motion Photogrammetry Reconstructions Using Small Unmanned Aerial Vehicles and Ground Photography to Estimate the Extent of Upland Soil Erosion." *Earth Surface Processes and Landforms*. 42,12: 1860-1871.

Kersten, Thomas & Lindstaedt, Maren. (2012). Image-Based Low-Cost Systems for Automatic 3D Recording and Modelling of Archaeological Finds and Objects. In: Ioannides M., Fritsch D., Leissner J., Davies R., Remondino F., Caffo R. (eds.) Progress in Cultural Heritage Preservation. EuroMed 2012. Lecture Notes in Computer Science, vol 7616. Springer Berlin, Heidelberg.

Knighton, David (1998). Fluvial Forms and Processes: A New Perspective. New York, NY: Oxford University Press Inc.

Kraft, T., Geßner, M., Meißner, H., Cramer, M., Gerke, M., and Przybilla, H.J. (2016). “Evaluation of a Metric Camera System Tailored for High Precision UAV Applications”. *The International Archives of the Photogrammetry, Remote Sensing and Spatial Information Sciences*. 1: 901-907.

Mancini, Francesco, Marco Dubbini, Mario Gattelli, Francesco Stecchi, Stefano Fabbri, and Giovanni Gabbianelli (2013). “Using Unmanned Aerial Vehicles (UAV) for High-Resolution Reconstruction of Topography: The Structure from Motion Approach on Coastal Environments.” *Remote Sensing*. 12: 6880–98.

Mayr, W. (2011). UAV mapping-a user report. ISPRS – Int. Arch. Photogramm. Remote Sens. Spatial Inform. Sci. XXXVII-1/C22, 277-282.

Nex, Francesco, and Fabio Remondino (2014). “UAV for 3D Mapping Applications: A Review.” Appl Geomat Applied Geomatics 6, no. 1: 1–15.

Radke, Richard J, Srinivas Andra, Omar Al-Kofahi, and Badrinath Roysam (2005). "Image Change Detection Algorithms: A Systematic Survey." *IEEE Transactions on Image Processing*. 14.3.

Rokhmana, Catur Aries (2015). “The Potential of UAV-Based Remote Sensing for Supporting Precision Agriculture in Indonesia.” *Procedia Environmental Sciences, The 1st International Symposium on LAPAN-IPB Satellite (LISAT) for Food Security and Environmental Monitoring*. 24: 245–53.

Rossi, Paolo, Francesco Mancini, Marco Dubbini, Francesco Mazzone, and Alessandro Capra (2017). "Combining Nadir and Oblique Uav Imagery to Reconstruct Quarry Topography: Methodology and Feasibility Analysis." *European Journal of Remote Sensing*. 50.1: 211-221.

Rosnell, Tomi, and Eija Honkavaara (2012). “Point Cloud Generation from Aerial Image Data Acquired by a Quadrocopter Type Micro Unmanned Aerial Vehicle and a Digital Still Camera”. *Sensors.* 12, no. 1: 453–80.

Shahbazi, Mozhdeh, Jérôme Théau, and Patrick Ménard (2014). “Recent Applications of Unmanned Aerial Imagery in Natural Resource Management.” *GIScience & Remote Sensing*. 51, no. 4: 339–65.

Snavely, N (2008). Scene reconstruction and visualization from internet photo collections, unpublished PhD thesis, University of Washington, USA

Suwardhi, D., F. Menna, F. Remondino, K. Hanke, and R. Akmalia (2015). “Digital 3D Borobudur - Integration of 3D Surveying and Modeling Techniques”. *ISPRS - International Archives of the Photogrammetry, Remote Sensing and Spatial Information Sciences.* 5: 417–23.

Toth, Charles, and Grzegorz Jóźków (2016). “Remote Sensing Platforms and Sensors: A Survey.” *ISPRS Journal of Photogrammetry and Remote Sensing, Theme issue “State-of-the-art in photogrammetry, remote sensing and spatial information science”.* 115: 22–36.

Torres, Jose Alberto, David Hernandez-Lopez, Diego Gonzalez-Aguilera, and Miguel Angel Moreno Hidalgo (2014). “A Hybrid Measurement Approach for Archaeological Site Modelling and Monitoring: The Case Study of Mas D’Is, Penàguila”. *Journal of Archaeological Science.* 50: 475–83.

Triggs W, McLauchlan P, Hartley R, Fitzgibbon A. (2000). Bundle adjustment – A modern synthesis. Eds W. Triggs, A. Zimmerman, and R Szeliski Vision Algorithms: Theory and Practice, LNCS, Springer Verlag, pp. 298-375.

Turner, Darren, Arko Lucieer, and Christopher Watson (2012). “An Automated Technique for Generating Georectified Mosaics from Ultra-High Resolution Unmanned Aerial Vehicle (UAV) Imagery, Based on Structure from Motion (SfM) Point Clouds.” *Remote Sensing Remote Sensing.* 4, no. 12: 1392–1410.

Uysal, M, A.S Toprak, and N Polat (2015). “DEM Generation with UAV Photogrammetry and Accuracy Analysis in Sahitler Hill”. Measurement 73: 539–43.

Westoby, M. J., J. Brasington, N. F. Glasser, M. J. Hambrey, and J. M. Reynolds (2012). “‘Structure-from-Motion’ Photogrammetry: A Low-Cost, Effective Tool for Geoscience Applications”. *Geomorphology*. 179: 300–314.

Xiang, Haitao, and Lei Tian (2011). “Development of a Low-Cost Agricultural Remote Sensing System Based on an Autonomous Unmanned Aerial Vehicle (UAV)”. *Biosystems Engineering.* 108, no. 2: 174–90.

APPENDIX A

OPUS REPORTS

```
                         NGS OPUS-RS SOLUTION REPORT
                         ==========================

All computed coordinate accuracies are listed as 1-sigma RMS values.
For additional information: https://www.ngs.noaa.gov/OPUS/about.jsp#accuracy

      USER: dbgallaw@uncg.edu                        DATE: April 04, 2017
RINEX FILE: 90c2070q.17o                             TIME: 18:08:46 UTC


  SOFTWARE: rsgps  1.37 RS59.prl 1.99.3           START: 2017/03/11 16:51:47
 EPHEMERIS: igs19396.eph [precise]                 STOP: 2017/03/11 17:36:23
  NAV FILE: brdc0700.17n                       OBS USED:  5166 /  5724   :  90%
  ANT NAME: TPSGR3          NONE              QUALITY IND.  28.45/ 56.62
ARP HEIGHT: 2.000                          NORMALIZED RMS:        0.333


 REF FRAME: NAD_83(2011)(EPOCH:2010.0000)             IGS08 (EPOCH:2017.19101)

         X:       920374.098(m)    0.004(m)           920373.257(m)    0.004(m)
         Y:     -5095485.456(m)    0.012(m)         -5095483.981(m)    0.012(m)
         Z:      3712117.692(m)    0.007(m)          3712117.593(m)    0.007(m)

       LAT:   35 49 10.38343       0.006(m)       35 49 10.41123       0.006(m)
     E LON:  280 14 19.24137       0.003(m)      280 14 19.21885       0.003(m)
     W LON:   79 45 40.75863       0.003(m)       79 45 40.78115       0.003(m)
    EL HGT:          243.965(m)    0.012(m)              242.609(m)    0.012(m)
 ORTHO HGT:          274.291(m)    0.020(m) [NAVD88 (Computed using GEOID12B)]

                      UTM COORDINATES     STATE PLANE COORDINATES
                       UTM (Zone 17)          SPC (3200 NC  )
Northing (Y) [meters]     3964642.245          229843.591
Easting (X)  [meters]      611895.663          540807.666
Convergence  [degrees]      0.72499232         -0.43941232
Point Scale                 0.99975428          0.99992159
Combined Factor             0.99971600          0.99988330

US NATIONAL GRID DESIGNATOR: 17SPV1189564642(NAD 83)


                              BASE STATIONS USED
PID       DESIGNATION                        LATITUDE     LONGITUDE DISTANCE(m)
DM3525 NCRE REIDSVILLE CORS ARP           N362142.714 W0793956.540   60790.6
DG5938 NCCA CARTHAGE CORS ARP             N352030.048 W0792305.085   63058.5
DK4045 NCTR TROY CORS ARP                 N352201.845 W0795212.770   51153.7
DL1894 NCWC WALNUT COVE CORS ARP          N362219.688 W0801105.625   72214.4
DG9328 DURH DURHAM COOP CORS ARP          N355946.129 W0785358.036   80230.6
DL3891 NCJL JORDAN LAKE CORS ARP          N354652.496 W0790203.927   65843.2
DN5840 NCSA SALISBURY CORS ARP            N354241.692 W0802555.994   61842.4
DK7549 NCST STATESVILLE CORS ARP          N355119.728 W0805055.477   98329.7
DM3527 NCRX ROXBORO CORS ARP              N362328.056 W0785954.418   93495.0

                    NEAREST NGS PUBLISHED CONTROL POINT
EZ1625      RA 7                          N354822.    W0794605.       1610.6
```

Figure 26. OPUS Report for GPS 1.

NGS OPUS-RS SOLUTION REPORT
==========

All computed coordinate accuracies are listed as 1-sigma RMS values.
For additional information: https://www.ngs.noaa.gov/OPUS/about.jsp#accuracy

USER: dbgallaw@uncg.edu DATE: April 04, 2017
RINEX FILE: 23f2070r.17o TIME: 18:05:39 UTC

SOFTWARE: rsgps 1.37 RS58.prl 1.99.3 START: 2017/03/11 17:46:30
EPHEMERIS: igs19396.eph [precise] STOP: 2017/03/11 18:31:29
NAV FILE: brdc0700.17n OBS USED: 5454 / 6300 : 87%
ANT NAME: TPSGR3 NONE QUALITY IND. 31.67/ 58.46
ARP HEIGHT: 2.000 NORMALIZED RMS: 0.334

REF FRAME:	NAD_83(2011)(EPOCH:2010.0000)		IGS08 (EPOCH:2017.19111)	
X:	920429.279(m)	0.003(m)	920428.438(m)	0.003(m)
Y:	-5095469.955(m)	0.018(m)	-5095468.480(m)	0.018(m)
Z:	3712115.325(m)	0.016(m)	3712115.226(m)	0.016(m)
LAT:	35 49 10.42456	0.006(m)	35 49 10.45235	0.006(m)
E LON:	280 14 21.51428	0.002(m)	280 14 21.49176	0.002(m)
W LON:	79 45 38.48572	0.002(m)	79 45 38.50824	0.002(m)
EL HGT:	238.164(m)	0.023(m)	236.808(m)	0.023(m)
ORTHO HGT:	268.490(m)	0.027(m)	[NAVD88 (Computed using GEOID12B)]	

	UTM COORDINATES UTM (Zone 17)	STATE PLANE COORDINATES SPC (3200 NC)
Northing (Y) [meters]	3964644.234	229844.421
Easting (X) [meters]	611952.684	540864.725
Convergence [degrees]	0.72536213	-0.43904792
Point Scale	0.99975444	0.99992159
Combined Factor	0.99971707	0.99988421

US NATIONAL GRID DESIGNATOR: 17SPV1195264644(NAD 83)

BASE STATIONS USED

PID	DESIGNATION	LATITUDE	LONGITUDE	DISTANCE(m)
DM3525	NCRE REIDSVILLE CORS ARP	N362142.714	W0793956.540	60781.3
DG5938	NCCA CARTHAGE CORS ARP	N352030.048	W0792305.085	63028.6
DK4045	NCTR TROY CORS ARP	N352201.845	W0795212.770	51166.0
DL1894	NCWC WALNUT COVE CORS ARP	N362219.688	W0801105.625	72243.3
DG9328	DURH DURHAM COOP CORS ARP	N355946.129	W0785358.036	80175.0
DL3891	NCJL JORDAN LAKE CORS ARP	N354652.496	W0790203.927	65786.2
DN5840	NCSA SALISBURY CORS ARP	N354241.692	W0802555.994	61898.6
DK7549	NCST STATESVILLE CORS ARP	N355119.728	W0805055.477	98386.6
DM3527	NCRX ROXBORO CORS ARP	N362328.056	W0785954.418	93452.3

NEAREST NGS PUBLISHED CONTROL POINT

EZ1625	RA 7	N354822.	W0794605.	1634.2

Figure 27. OPUS Report for GPS 2.

APPENDIX B

TOTAL STATION SURVEY

Table 31. Total Station Survey Data for the Native Son Vineyard

Name	Northing	Easting	Elevation	Description
3	229805.6	540812	271.6542	GCP
4	229809.4	540776.3	274.2652	GCP
5	229807	540793.9	273.1685	GCP
6	229804.9	540830.3	270.5027	GCP
7	229805.1	540848.1	269.0136	GCP
8	229806	540866.1	267.8672	GCP
9	229848.7	540808.4	274.2618	GCP
10	229849.9	540825.6	272.7696	GCP
11	229851.7	540789.6	276.6308	GCP
12	229849.9	540825.6	272.7679	GCP
13	229838.3	540862.8	268.5793	GCP
14	229839.6	540881.1	266.3254	GCP
15	229808.1	540884.6	267.1241	GCP
16	229808.7	540902.2	266.7106	GCP
17	229807.9	540920.3	266.8773	GCP
18	229839.7	540898.6	264.9008	GCP
19	229838.1	540916.9	264.8184	GCP
20	229869.1	540913.1	263.4134	GCP
21	229820.8	540933.6	266.5705	GCP
22	229851.8	540929.5	265.0746	GCP
23	229870.5	540927.6	263.9275	GCP
24	229870.2	540895.6	264.1812	GCP
25	229871	540877.5	266.3036	GCP
26	229870.7	540859.6	267.9879	GCP
27	229875.7	540852.9	268.2732	GCP
28	229895.5	540838.2	271.4204	GCP

29	229850.1	540843	270.9489	GCP
30	229896.5	540820.6	273.6156	GCP
31	229896.5	540803	275.2546	GCP
32	229898.1	540785	277.4076	GCP
33	229899.1	540767.3	278.8879	GCP
34	229853	540771.7	278.4904	GCP